



TECHNISCHE
UNIVERSITÄT
WIEN

Vienna University of Technology

D I P L O M A R B E I T

Simulation studies for the Bragg peak determination using prompt gamma rays in ion therapy

ausgeführt an der
Österreichischen Akademie der Wissenschaften

unter der Anleitung von
Privatdoz. Dipl. Ing. Dr. Johann Marton

durch
Andreas Pichler

Keramikstraße 459
3511 Furth

Datum

Unterschrift

Note of thanks

First and mainly I want to thank my family, whose never ending financial and human support made it possible for me to finish my studies, although it took a bit longer than expected. I will never forget that. Also I want to thank my supervisor at the Stefan-Meyer Institute Dr. Johann Marton, who spent much time on answering my questions and thinking about my problems. Special thanks of course also goes to Dr. Albert Hirtl and Dipl.-Ing. Hermann Fuchs from the AKH, who always answered my questions (also if they were dispensable) and never lost their nerves, even during the longest discussing sessions. Furthermore, I want to thank Dr. Paul Bühler, whose knowledge of pretty much everything helped a lot. Last but not least, I want to thank BSc. Dominik Steinschaden, who worked on the prompt gamma project with me and whose ideas have always been inspiring.

Kurzfassung

In der Strahlentherapie mit Ionen gibt es keine zufriedenstellende Methode um die Reichweite der Ionen in Echtzeit zu überprüfen. Das PET Monitoring, welches in einigen Einrichtungen zu diesem Zweck installiert wurde, hat einige Nachteile. Deswegen werden neue Methoden untersucht, wie zum Beispiel die Detektion von prompt emittierten γ -Photonen. Diese Photonen werden entlang des ganzen Pfades der Ionen von angeregten Target- und Projektilteilchen emittiert, mit einem Maximum der Emission in der Region des Bragg-Peaks in den meisten Energiebereichen. Durch dieses Maximum sollte der Bragg-Peak und damit auch die Reichweite der Ionen im Target bestimmt werden. Dieser Umstand wurde mittels der Gate Simulationsumgebung untersucht. Die Winkelverteilung der Photonen wurde gemessen mit dem Ergebnis, dass mehr Photonen in Strahlrichtung gemessen werden als in die Gegenrichtung für einen Großteil der Energiebereiche der Photonen. Die Reichweite der Ionen wurde berechnet indem prompte Photonen außerhalb eines Wassertargets mittels zylindrischer Bleikollimatoren und zylindrischer Detektoren gemessen wurden. Die endliche Länge der Kollimatoren, die Septenpenetration und Absorptionseffekte im Target wurden durch eine Responsefunktion berücksichtigt, welche die Photonenproduktion und die Photonendetektion verband. Die Genauigkeit der Berechnung der Reichweite der Ionen war zu einem großen Teil von den Fehlern dieser Responsefunktion abhängig und der relative Fehler lag zwischen 0 % und 5 %, abhängig von der Primärenergie.

Abstract

In the radiation therapy with ions, no satisfying method exists for real-time range monitoring. The PET monitoring, which is implemented in a few facilities for this purpose, has its drawbacks. This is why new methods are under investigation, like the detection of promptly emitted γ - photons. These photons are emitted all along the ion path from excited target and projectile particles, with a maximum of the emission in the region of the Bragg peak for the most photon energies. By this maximum, the Bragg peak depth and with that, the ion range should be identified. This circumstance was investigated using the Gate simulation framework. The angle distribution of the photons was measured with the result, that more photons are detected in forward direction than in backward direction for a majority of the photon energy ranges. The ion range was calculated by detecting the prompt photons outside of a water target using cylindrical lead collimators and cylindrical detectors. The finite collimator length, the septal penetration and absorption effects in the target were taken into account by a response function, which linked the photon production with the photon detection. The accuracy of the calculation of the ion range largely depended on the errors of this response function and the relative error varied between 0 % and 5 %, depending of the primary ion energy.

Contents

1	Introduction	1
2	Physical aspects	3
2.1	Prompt γ - photons	3
2.2	PET monitoring	4
2.3	Ionizing radiation	5
2.3.1	Interaction of ionizing photons with matter	5
2.3.2	Interaction of ionizing particles with matter	8
2.4	Particle accelerators	10
2.4.1	Linear particle accelerator	10
2.4.2	The cyclotron	11
2.4.3	The synchrotron	12
2.4.4	MedAustron	13
3	Biological aspects	15
3.1	Relative biological effectiveness	15
3.2	Other dependencies of the biological effect of radiation	16
4	Gate	17
4.1	Building a Gate simulation	17
5	Depth of the Bragg peak	21
5.1	Dose distribution in water	22
5.2	Dose distribution in other materials	23
5.3	Verficiation of simulations	24
6	Angular distribution	27
6.1	Angular dependence	30
6.1.1	Other materials	34
6.2	Dependence on photon energy	35

7	Detection of the Bragg peak	43
7.1	Without collimators	43
7.2	Ideal collimators	47
7.2.1	Calculation of the response function	50
7.2.2	Calculation of the Bragg peak	54
7.3	Realistic collimators	60
7.3.1	Calculation of the response function	61
7.3.2	Calculation of the Bragg peak	72
7.3.3	Optimization of the geometry	74
7.3.4	Results for different primary ion energies	78
8	Summary and outlook	87

1 Introduction

In radiation therapy with ions, there is currently no satisfying real time monitoring of the dose application (Positron Emission Tomography - Monitoring see chapter 2.2). The exact location of the malignant tissue is determined prior to the therapy with a CT or MRT and the parameters of the radiation (energy, exposure time, ...) are computed with the help of these results. But during the application of the dose, it is not (or not satisfactorily) possible to determine whether the targeted tissue is irradiated or not. It is particularly interesting to study this problem, as a new facility for ion therapy is currently under construction in Wiener Neustadt near Vienna. It is called MedAustron and protons and carbon ions will be used to treat cancer. At MedAustron, there also will be the need of an online treatment monitoring.

A new scheme to solve this problem is the dose verification by detection of promptly emitted γ - photons during the irradiation. The basic idea is, that more of the photons, which originate from the impact of the primary ions, are produced in the region of the Bragg peak. If it is possible to detect these photons and determine their origin, it should be possible to calculate the position of the Bragg peak. The feasibility of this approach was shown experimentally in [1], by moving a slit collimator along the beam axis on top of the irradiated object.

The goal of this work was to develop a method based on Monte Carlo simulations to detect the Bragg peak more efficiently based on information from prompt photons. These simulations were performed using the framework Gate, which is capable of simulating setups used in ion therapy.

2 Physical aspects

2.1 Prompt γ - photons

During the irradiation in proton and ion therapy, secondary particles are produced. This includes prompt emission of particles like photons and neutrons or delayed emission of radiation from unstable nuclei. The prompt emission of photons is due to fragmentation reactions which produce excited nuclei which occur along the stopping path of the primary ions [2]. This process is displayed in figure 2.1. In the first step of this reaction, the

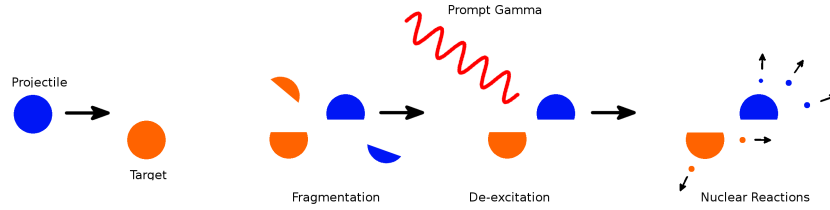


Figure 2.1: Production mechanism of prompt photons.

primary particle and the target nuclei collide with each other leading to a fragmentation. The resulting nuclei are excited and de-excite on a time scale of typically 1 ns [2]. The resulting radiation is called prompt gamma radiation. Since these fragmentation reactions occur all along the ion path [1], prompt photons are produced all along the ion path. Consequently, the detection of these promptly emitted photons could be used to monitor the range of the ions and with that the position of the Bragg peak. Additionally, the detection of prompt gammas does not have the same problem of the delusion of the signal due to physiological processes as the PET monitoring (see section 2.2), because of the mentioned very small time until its emission. In [1] it has been shown experimentally, that the prompt photons emitted orthogonally to the beam exhibit a peak structure which is correlated to the Bragg peak.

2.2 PET monitoring

PET (Positron Emission Tomography) monitoring is currently the only technically feasible non invasive technique to verify the projectile range and the position of the Bragg peak in ion therapy [3]. It is based on the detection of photons, which originate from the activation and β^+ emission of either target or projectile particles. The β^+ particles then annihilate with electrons in the target and send out a pair of photons. Typical positron emitters are for example the isotopes ^{11}C and ^{10}C , which originate from the primary therapeutic ^{12}C ion beam. Other secondary lower mass fragments (e.g. hydrogen, helium) are responsible for the dose tail behind the Bragg peak in the therapy with heavy ions [2]. For protons, there is no tail like that, because of the lack of these secondary fragments. Activated target material stays in its place until the positron emission, whereas activated projectiles travel until the end of their range until they emit the positron [3]. A distribution of activation in the case of a carbon ion irradiation of a PMMA (Polymethyl methacrylate also called Plexiglas) target with an energy of 212 MeV/u as a function of penetration depth compared to a distribution of the dose is shown in figure 2.2. It can be seen, that

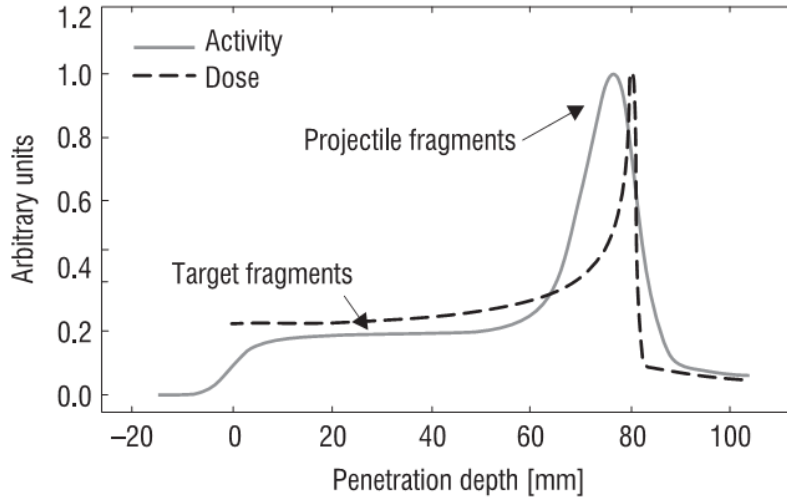


Figure 2.2: Comparison between activation and dose as a function of depth in a PMMA target during carbon ion therapy at $E = 212$ MeV/u [3].

the peak of activity is slightly before the Bragg peak and is due to positron emitting projectile fragments [3]. In the case of a proton beam, this peak structure is missing because of the lack of secondary fragments. Treatment verification can be obtained by comparing the acquired data to expectations based on the treatment plan. The emission of this radiation, which is caused by the emission of positrons, is delayed because of the half lives of the involved reaction products (e.g. ^{15}O , ^{10}C , ^{11}C), which can range from a few

seconds to several minutes. Therefore the signal can be measured during or shortly after the irradiation. 3 different kinds of implementations are distinguished:

in-beam PET: The “in-beam” PET is a data acquisition in the course of the irradiation, in between single pulses of the irradiation. These solutions are restricted to limited angle detectors with lower efficiency [2].

in-room PET: In the case of an “in-room” PET, the data acquisition starts right after the irradiation.

offline PET: And “offline” PET monitoring is conducted with the help of a full ring PET scanner outside of the treatment room. This solution has a better image performance, but valuable short lived isotopes are lost (e.g. ^{15}O). Another drawback of this technique is, that the positron emitting isotopes can be transported away from their original position through physiological processes, due to the long time between irradiation and PET scan. This is called the “wash-out effect” [2].

2.3 Ionizing radiation

Radiation which has enough kinetic energy to liberate an electron from the bond of the atom is called ionizing radiation. On the one hand this radiation can consist of photons with different energies from x-rays to gamma rays. The UV region is considered to be the transition area from ionizing to non-ionizing radiation [4]. Electromagnetic radiation below the UV does not carry enough energy to ionize atoms. On the other hand ionizing radiation can also consist of particles like alpha or beta radiation with enough kinetic energy.

2.3.1 Interaction of ionizing photons with matter

There are several different interactions of photons with matter namely:

Compton effect: In the Compton effect a photon interacts with a loosely bound electron in an outer shell of an atom and transfers a part of its energy to the electron, breaking it loose from the bond to the atom. The photon is not absorbed by this effect but is deflected by an angle θ , which is given in equation (2.1) [5].

$$\lambda_s = \lambda_0 + \frac{2h}{m_e c} \sin^2\left(\frac{\theta}{2}\right) \quad (2.1)$$

In this equation, λ_0 and λ_s are the wavelengths of the photon before and after the scattering, h is the Planck constant, m_e is the rest mass of the electron, c is the

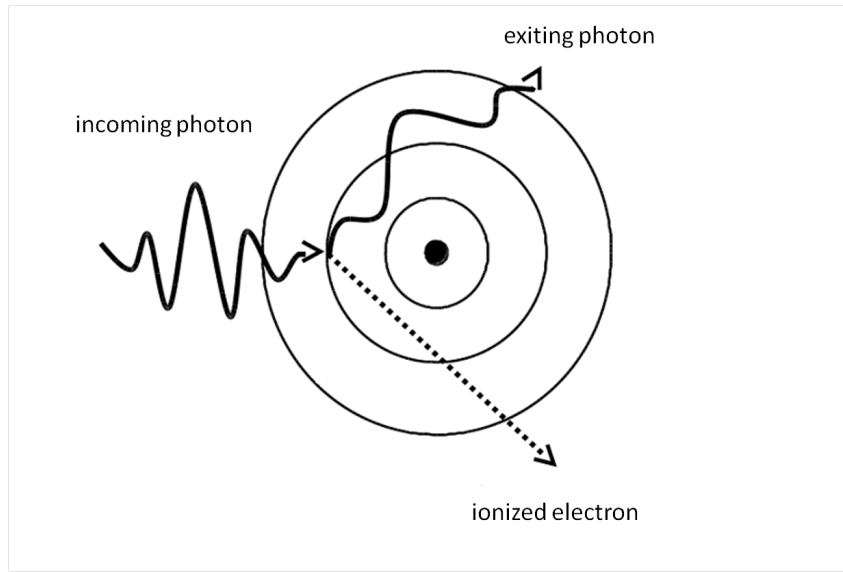


Figure 2.3: Compton effect [4]

speed of light and θ is the deflection angle. The effect is pictured in figure 2.3.

Photoelectric effect: In the photoelectric effect a photon transfers its energy to an electron of an energetically deep shell and ionizes this electron. The photon is absorbed in the course of this process. The electron then moves with the energy of the photon minus the energy which was necessary to ionize the electron [5]. The process is displayed in figure 2.4.

Pair production: At photon energies higher than 2 times the rest mass of an electron (0.511 MeV), pair production can occur. In this mechanism, the photon interacts with a target nucleus, which absorbs a bit of the photons momentum, and its energy is converted into an electron/positron pair, generating mass according to $E = mc^2$. Both particles have the same kinetic energy $E_{\text{kin}} = \frac{E_{\text{photon}} - 2m_e c^2}{2}$ [5].

Additional to these 3 processes, there is also elastic scattering of photons, where the incoming photons excites the electron to oscillate with the photon's frequency. The electron then radiates an electromagnetic wave with the same frequency as the incoming photon,

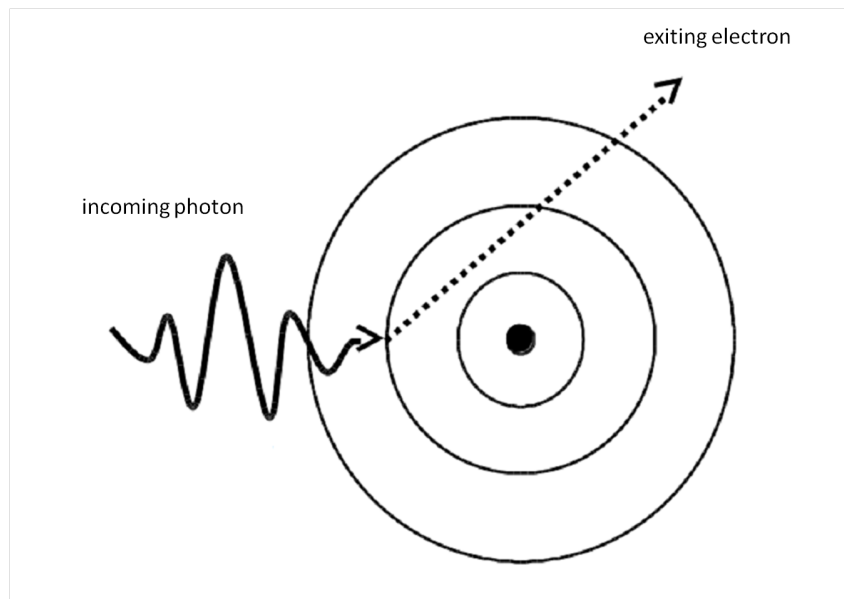


Figure 2.4: Photoelectric effect [4]

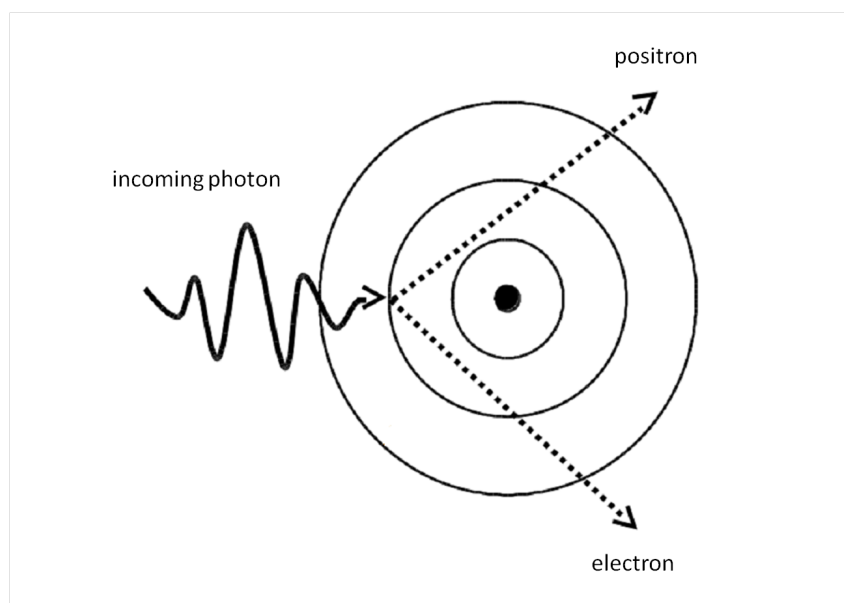


Figure 2.5: Pair production [4]

but the electron itself does not change its energy state. This process only plays a role at photon energies below about 10 keV, which is why it is not important for radiology [4]. For low photon energies, the photoelectric effect has the highest probability. For slightly higher energies, the Compton effect is most abundant and for still higher energies, the pair production is dominating. [5]

When a collimated beam of photons with the intensity P_0 passes through a layer of matter with the thickness dx , a detector behind the target right in the line of the beam detects the intensity $P(x)$.

$$dp = P(x) - P_0 = -\mu P(x) dx \quad (2.2)$$

The difference between these 2 intensities dp is given in equation (2.2), where μ is the attenuation coefficient of the material. Integration of this formula over a thickness x yields equation (2.3) [5].

$$P(x) = P_0 e^{-\mu x} \quad (2.3)$$

The reasons for the attenuation are the absorption and scattering through the above mentioned effects in the material. In radiation therapy with high energy photons, the depth-dose distribution also follows an exponential decrease, after an initial dose build up, which is due to forward scattered Compton electrons [2]. This build up shifts the peak of the dose a few centimeters away from the surface of the patient's body. The depth dose distribution is pictured in figure 2.6. This distribution has the disadvantage, that the dose does not exhibit a peak structure, as it is the case for ions. Therefore an irradiation of the tissue surrounding the target volume can not be avoided.

2.3.2 Interaction of ionizing particles with matter

Accelerated ions with therapeutically interesting energies get stopped in the target material predominantly through Coulomb interaction between them and the electrons in the target atoms [6]. These interactions lead to excitation and ionization of the electrons along the ion path. The energy loss per length of ions is described by the Bethe formula, which is given in equation (2.4) [6].

$$\frac{dE}{dx} \approx \frac{Kn_0(Z_{eff})^2}{\beta^2} * [\ln \frac{2m_e c^2 \beta^2}{I(1 - \beta^2)} - \beta^2] \quad (2.4)$$

Here $\frac{dE}{dx}$ is the energy loss per length, K is a constant, n_0 is the electron density in the target, Z_{eff} is the effective charge of the projectiles, $\beta = \frac{v}{c}$ is the velocity in units of the speed of light, I is the mean ionization energy of the target and m_e is the rest mass of

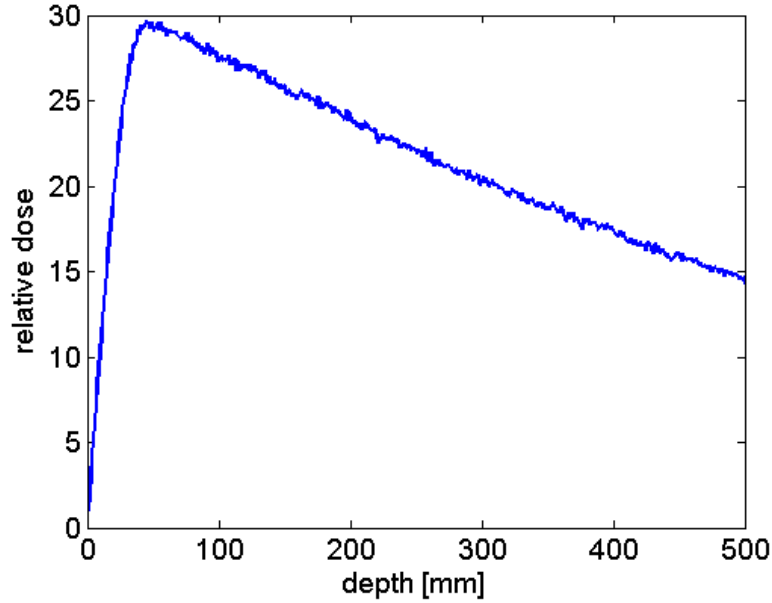


Figure 2.6: Simulated depth-dose distribution for 10 MeV photon radiation in water.

the electron. So the energy loss per length (also called “stopping power”) is proportional to $\frac{Z_{\text{eff}}^2}{\beta^2}$. Because of the dependence on $\frac{1}{\beta^2}$, the stopping power increases with decreasing energy. At high velocities, the ions are completely stripped off their electrons, and the effective charge is equal to the number of protons Z [2]. For smaller energies, the ion acquires electrons through recombination processes, decreasing the effective charge Z_{eff} . Through the interaction of these 2 effects, the stopping power has a maximum at a finite energy, this energy being about 350 keV/u for carbon ions [2]. This is the energy the ions have at the Bragg peak. At still lower energies elastic collisions with the target nuclei start to play a role in the slowing down process of the ions. But as the range with this energy is in the order of just a few μm (see also figure 2.7), this does not play a role and this contribution is often neglected in radiotherapy applications. The stopping power as a function of the ion energy is shown in figure 2.7. As heavy ions are not much deflected and travel almost on a straight line, the length of the trajectory of the particle is almost the same as the mean traversed absorber thickness. Nevertheless, fluctuations in the number of collisions in a beam consisting of many particles cause slight difference in the ions ranges [6]. This phenomenon is called range straggling and it leads to a broadening of the Bragg peak. For heavier ions, this effect varies approximately with $\frac{1}{\sqrt{M}}$ with M being the mass of the particle [6]. Thus heavier ions exhibit less range straggling than lighter ions. Also lateral beam spreading occurs, which is predominantly due to elastic Coulomb interactions with the target nuclei [2]. This effect also increases with decreasing particle

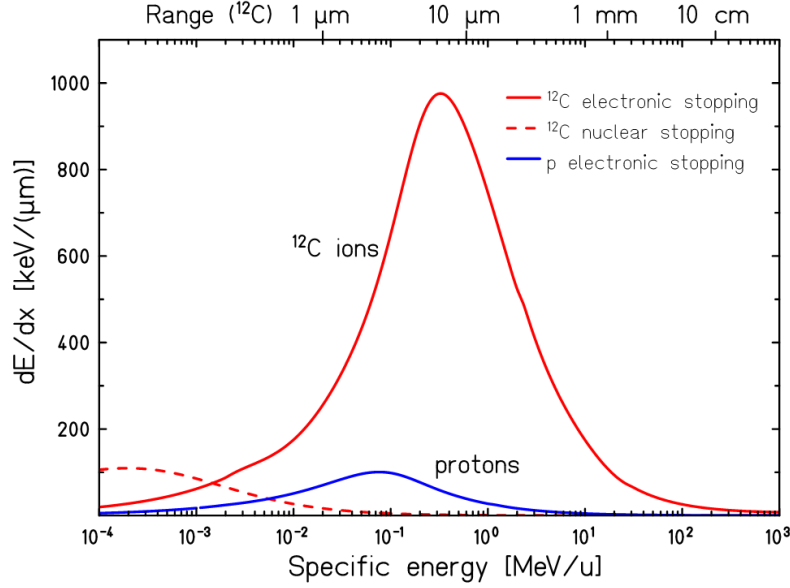


Figure 2.7: Stopping power for carbon ions and protons in water as a function of the energy, also shown is the range of the ions corresponding to their specific energy [2].

mass. Additionally, it increases with decreasing particle energy and with increasing Z of the target nuclei [2]. That is why heavy ions show a small lateral beam spread, which is useful for irradiation near organs at risk.

2.4 Particle accelerators

Particle accelerators are needed to generate the high energy ion radiation used for therapeutic purposes. There are several types of particle accelerators.

2.4.1 Linear particle accelerator

There are 2 different types of linear accelerators (LINAC):

Drift-tube LINAC:

This type of LINAC consists of a series of cylindrical tubes, which are all connected to a high frequency power supply. A schematic picture of the setup is given in figure 2.8. The connection of the high frequency oscillator and the electrodes is in the way,

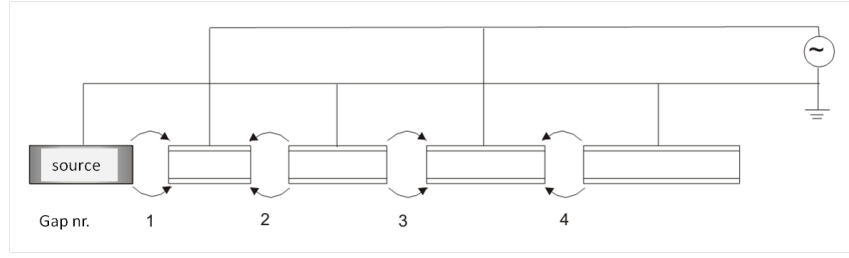


Figure 2.8: Schematic picture of a drift-tube LINAC [7].

that consecutive tubes have opposing polarities. The particle beam is injected into the vacuum chamber along the axis. Inside the chamber, the electric field is always equal to 0. In between single chambers, the field changes with the frequency of the oscillator. The length of the electrodes is chosen in the way, that an electron, which experiences an acceleration in the right direction between the first 2 chambers, passes a chamber in half a period of the oscillator. That way, the acceleration of the particle is the same in every gap. The particle gains the energy qU at every acceleration, when q is its charge and U is the voltage in the gap at the moment the particle passes through it. The length of a single vacuum chamber $l = v \frac{T}{2}$, where T is the period of the oscillator and v is the particle velocity, which is required for the particles to be accelerated in every gap, increases with increasing length of the particle track, because of the increasing velocity v . For v approaching c , the length becomes constant, since the velocity v becomes constant. This type of accelerator is used predominantly to accelerate protons and ions [7].

Travelling-wave LINAC:

For this kind of accelerator, the fact is used, that in a waveguide, a propagating electromagnetic wave is not purely transversal, but also has a component in propagation direction [8]. This component is used to accelerate the particles in the tube continuously. This device is mostly used for particles, which were already accelerated to almost the speed of light (e.g. electrons).

2.4.2 The cyclotron

In a cyclotron, charged particles are accelerated with an electric high frequency field. Their track has the form of spirals, in which they are forced through a magnetic field orthogonal to their path. A schematic picture of a cyclotron is given in figure 2.9. The particle is ejected from the particle source and gets accelerated by the electrical field into one of the flat, evacuated half-cylinders, which are called “Dee” due to their shape,

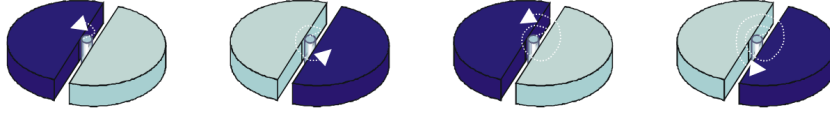


Figure 2.9: Schematic picture of a cyclotron [7].

in which the electrical field is equal to 0. The electrical polarisation of the 2 “Dees” is represented by different colours in the plot. In the first half-cylinder, the particle is forced on a circular path by the magnetic field, which is orthogonal to the particle track. When it reaches the gap again, it is accelerated into the other “Dee” by the electric field and the now more energetic particle again runs through a circular path with a larger radius than before until it reaches the gap and so on. The acceleration in the gap is achieved by making the time the particle needs to pass through a “Dee” exactly half of the period of the oscillating electric field in between the gaps. So it is again ensured that the particle is accelerated during every passage of the gap. The angular frequency ω for this condition is given in equation (2.5).

$$\omega = \frac{|q|B}{m} \quad (2.5)$$

Here q is the charge of the particle, m is the mass of the particle and B is the magnetic field. The angular frequency consequently depends on the mass of the particle. As the mass is increasing for relativistic particles, the angular frequency is not the same any more for all particle energies and also not for all the particles which are in the cyclotron at the same time. This limits the energy for protons for example to about 20 MeV [7], because otherwise the particles would get too heavy. Electrons can not be accelerated with this type of accelerator, because relativistic effects occur at low energies. A solution to this problem is to decrease the frequency of the oscillator during the acceleration of one particle package, according to the decrease of the angular frequency due to the relativistic increase of mass (synchro-cyclotron).

2.4.3 The synchrotron

The synchrotron is a particle accelerator, in which the particles are accelerated by a high frequency electric field and are kept on a circular track by a magnetic field which is orthogonal to the particle track. A schematic picture of a synchrotron is shown in figure 2.10. The vacuum chamber of the synchrotron has the form of a torus, with the high frequency alternating voltage source being located on one spot of the ring. The high voltage is generated by stationary electromagnetic waves in the cavity [7]. The period of the alternating voltage has to be equal to the time, a particle needs to go around the whole

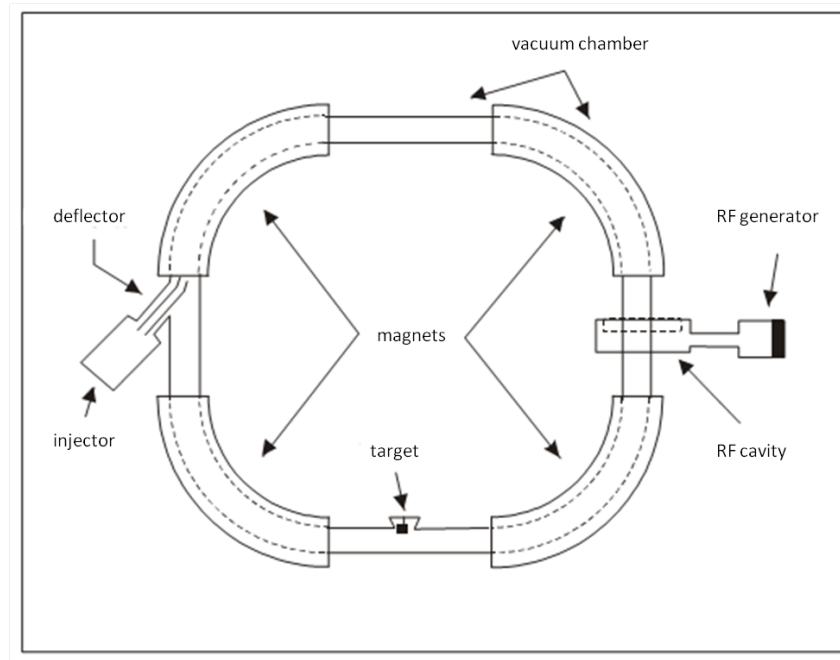


Figure 2.10: Schematic picture of a synchrotron [7].

circle (or a submultiple). Due to the increasing particle energy during the acceleration process, this frequency has to be increased with time.

$$R = \frac{m * v}{|q|B} = const \quad (2.6)$$

Equation (2.6) follows directly from the equality of centrifugal and centripetal force on a circular track. For the circular radius R to be constant, the magnetic field also has to increase, because the velocity and the mass of the particle also increase. To avoid a great modulation of the radio frequency, the particles are often injected to the synchrotron (e.g from a LINAC) with an energy of a few MeV [7].

2.4.4 MedAustron

MedAustron is a new particle accelerator which is currently under construction in Wiener Neustadt. The general setup is shown in figure 2.11. It consists of a linear accelerator, which accelerates the ions coming from an ion source and injecting them into a synchrotron. The synchrotron then accelerates the ions to an upper limit of 400 MeV/u for carbon ions and to 800 MeV for protons. These are the 2 types of ions which are planned to be used from the start. Helium ions are also considered to be added at a later stage. Then the ions are extracted from the synchrotron and directed into one of the clinical treatment

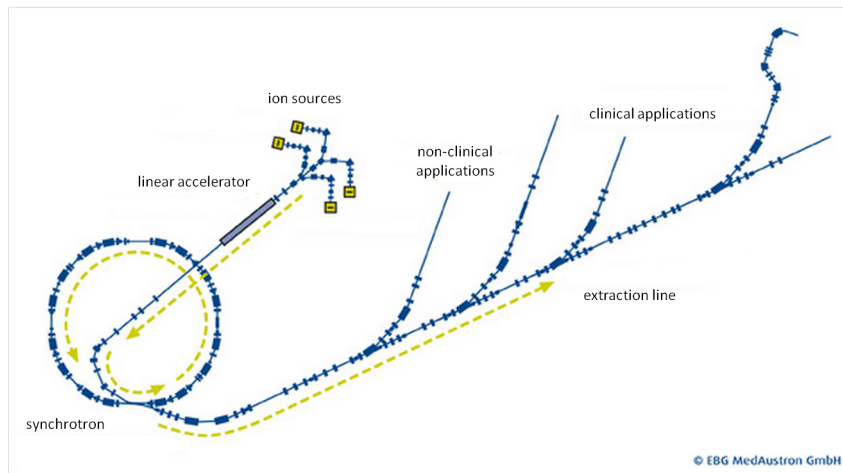


Figure 2.11: MedAustron accelerator with beamlines for clinical and non-clinical applications [9].

rooms (ion therapy for cancer) or in the room for non-clinical applications (pure research in radiobiology and radiation physics) [9].

3 Biological aspects

3.1 Relative biological effectiveness

Relative biological effectiveness (RBE) is the ratio between the dose of a reference radiation which is needed to achieve a certain biological effect to the dose which is needed to achieve the same effect with the radiation currently under investigation (e.g. ion radiation) [2]. As a reference radiation typically γ -rays or X-rays are chosen. The biological effect which should be achieved is often taken to be a certain amount of cells not surviving the irradiation, since this is a good measure for the ability of this radiation to kill cancer cells. Studies showed, that protons in the important energy ranges have a relative biological effectiveness of about 1, meaning that the same dose needs to be delivered to achieve the same effect as with photon irradiation [6]. An elevated RBE has been found for the Bragg peak region of ions heavier than helium compared to the region in front of the Bragg peak and compared to photon irradiation. This is caused by the elevated LET (Linear Energy Transfer, a parameter related to the stopping power) of heavy ions at the end of their range (see section 2). The increased value of the LET for heavier ions is because of the proportionality to Z_{eff}^2 in the equation (2.4). The higher the Z of the ion, the higher the possible Z_{eff} values.

The larger radiation damage caused by ions can also be explained by the different microscopic dose distributions of ions and photons. Photons exhibit a rather homogeneous dose distribution, whereas for ions the track center of single ions is only a few nanometers broad [2]. The cell nucleus is the most fragile part of the cell, and it is easiest to affect the capability of the cell to perform cell division with damages to the nucleus and specifically with damages to the DNA in the nucleus [4]. The former considerations lead to a high probability of correlated DNA damage (e.g. double strand breaks) for ion irradiation, whereas for photon radiation, the distance between single damage sites is higher. Since the repair capability is smaller for complex, correlated DNA damage as caused by ions, the biological damage is more severe for ion irradiation.

In general one can distinguish between *direct* DNA damage through the radiation or its surrounding secondary electrons, which is the smaller part of the damage. And *indir-*

ect DNA damage, which is caused by radiation induced radicals, contributing the larger part to the radiation damage [2].

3.2 Other dependencies of the biological effect of radiation

Apart from the dependence of the biological effect of radiation on the LET and the spatial dose distribution of different kinds of radiation, which was discussed above, it also depends on the amount of oxygen in the irradiated cell. During tumor growth, new blood vessels have to be built to transport oxygen to the cells. As the growth is a fast process, the building of new vessels is often insufficient, which results in an insufficient supply of the tumor cells with oxygen [2]. A lower oxygen status in turn results in a higher resistance of the cells to radiation. The reason for this effect is yet to be determined. The effect is described with the help of the oxygen enhancement ratio (OER), which is defined in equation (3.1).

$$\text{OER} = \frac{D_{\text{hypoxic}}}{D_{\text{aerob}}} \quad (3.1)$$

The OER is the ratio between the dose for hypoxic cells to the dose for aerob cells, which is needed to produce the same biological effect [2]. It is about 3 for conventional photon radiation and significantly smaller in the case of ion irradiation. Predominantly in the high LET regions (e.g. Bragg peak region) it is close to 1. For the radiation of hypoxic tumor entities, these facts represent an advantage of ion radiation over conventional radiation.

The biological effect of photon radiation also depends on the phase of the cell division the irradiated cell is in [6]. It is most vulnerable to radiation in the so-called G1-phase, which directly follows the mitosis. This effect also occurs for ion radiation, but it is much less pronounced. Furthermore the biological effect depends on the intensity of the radiation as a function of time (e.g. low dose over a long time or high dose over a short time), because of repairing processes in the cells and on the kind of the cells [4].

4 Gate

Gate is the abbreviation for Geant4 Application for Tomographic Emission [10]. It is an open source software developed by the international OpenGATE collaboration and dedicated to numerical simulation in medical imaging and radiotherapy. Furthermore it is the software which was used in the course of this work. It is based on Geant4, which is a toolkit for simulating the passage of particles through matter, implemented in the C++ programming language. It includes hadronic, electromagnetic and optical processes within a wide energy range [11].

4.1 Building a Gate simulation

Several steps have to be taken when building a Gate simulation.

Defining a material database:

At first a material database has to be set with the command `/ gate / geometry / setMaterialDatabase`. In this database, all the materials are stored which can be used to build the simulation. Some of them will be utilized extensively in the following parts of this work, such as: water, lung tissue, brain tissue, skull and lead. For some important materials, like water, there are more thorough definitions. This second definition of water is called “G4.water” and it includes for example a table with the experimentally measured stopping power, which the first definition does not. This more thorough definition of water was used in the course of this work. The database which was utilized is called “GateMaterials.db”.

Defining a geometry:

New volumes in the simulations have to be built as so called “daughters” of another volume with the help of the command `/ gate / ‘‘mother volume name’’ / daughters / name`. This means that its position is always defined relative to the middle of the “mother” volume. In the beginning, the only volume existing is the “world”, whose dimensions need to be specified. It is not possible to build volumes outside of the “world”. Volumes

can be built in various shapes, such as cylindrical, spherical or cubic for example.

Defining physical processes:

This is done by including a library of physical effects. The name of the library was “hadrontherapyStandardPhys.mac” and it was taken from [12]. It is possible to manually deactivate single unwanted effects or set cuts.

Defining output:

This is done by attaching so called “actors” to volumes in the simulation. Actors are tools in Gate which record information about the physical processes going on in the volume they are attached to. There are various types of actors and depending on the type, the output differs. These types are the following [13]:

Dose Actor: This actor records the dose in the volume it is attached to in the unit Gray [$\frac{J}{kg}$]. It can be separated into voxels, and record the dose for each voxel. The output can be given in the ASCII or ROOT format, for example. The ROOT system is an object oriented framework for large scale data analysis, which is written in C++ [14]. This actor can also record the number of particle hits and the deposited energy.

Spectrum Actor: It records the energy spectrum for a certain kind of particle in the volume it is attached to. The binsize and the upper and lower bound of this spectrum can be set in advance. The output is a ROOT file.

Kill Actor: This actor extinguishes every particle of a certain kind when it interacts for the first time in the volume it is attached to. The output is an ASCII file with the number of extinguished particles.

Production and Stopping Actor: This actor can also be separated into voxels, and it counts the number of particles produced and the number of particles stopped in each voxel. The output file can be in ASCII or ROOT format.

There are several more actors, but these were the important ones for the following work. On every actor, filters can be applied. For example the energy filter lets the actors only see particles in a specified energy range. Or the particle filter lets the actors only record data from a special kind of particle.

Initialize the simulation:

After these steps, the simulation needs to be initialized. This is done with the Gate command `/ gate / run / initialize`.

Defining a source:

The parameters that have to be specified here are the emitted particle type, the particle energy (or energy distribution), the position of the source, the shape of the beam (or the angular distribution of the primary particles), the shape of the source and the number of primary particles. In this work, the primary particles were always either carbon ions or photons. Furthermore, the shape of the beam was set to be point like in chapter 5 and for all following chapters, the beam had a Gaussian shape with a sigma of 3 mm, in order to be closer to reality.

Start the simulation:

This is done by the command `/ gate / application / startDAQ`.

5 Depth of the Bragg peak

In the introduction it was mentioned, that the main goal of this work was to identify the depth of the Bragg peak by detecting promptly emitted photons. To get to that goal, several steps were taken. At first, the depth of the Bragg peak was measured by measuring the depth-dose distribution in the target. This was done, for example, to verify the results obtained by calculating the Bragg peak position with the information of detected photons. Then the angular distribution of the promptly emitted photons was investigated, to get a knowledge of where it would be best to put the detector relative to the target. Then finally, a concept of a setup for detecting the depth of the Bragg peak was simulated. This chapter is about measuring the depth-dose distribution and with that the Bragg peak depth inside of the target.

The depth of the Bragg peak was of importance for this work for several reasons. First, it was interesting to know about the behaviour of the Bragg peak position as a function of the primary ion energy and how it changes with varying target material. The second reason was, that the angular distribution of the emitted photons also needed to be measured in the course of this work. For this purpose, a spherical target with the Bragg peak in its center had to be built. To do that, the depth of the peak and along with that, the dose distribution, had to be known. The setup of the simulation to measure the depth of the Bragg peak is shown in figure 5.1. In this plot, the carbon ion beam is hitting the target from the left hand side. The phantom is a homogeneous cylinder consisting of varying materials (but only one material for each simulation), with a radius of 30 cm and length of 70 cm. The penetration depth is measured of course starting from the beginning of the cylinder, as marked in the plot. In the simulation, a *Dose Actor* was connected to the phantom. A *Dose Actor* measures the deposited dose with an adjustable spatial resolution (see also section 4). The resolution in these simulations was set to 1 mm in the direction of the beam. In the direction orthogonal to the beam, the volume was not separated into voxels. The actor measured the deposited dose per millimeter depth in Gray [$\frac{J}{kg}$]. In the following the Bragg peak will be identified as the place of the maximum dose. An example for the Gate source code for this kind of actor is given in listing 5.1. In this listing, a *Dose Actor* is attached to the volume *human*, which is the target, and the voxel size is adjusted.

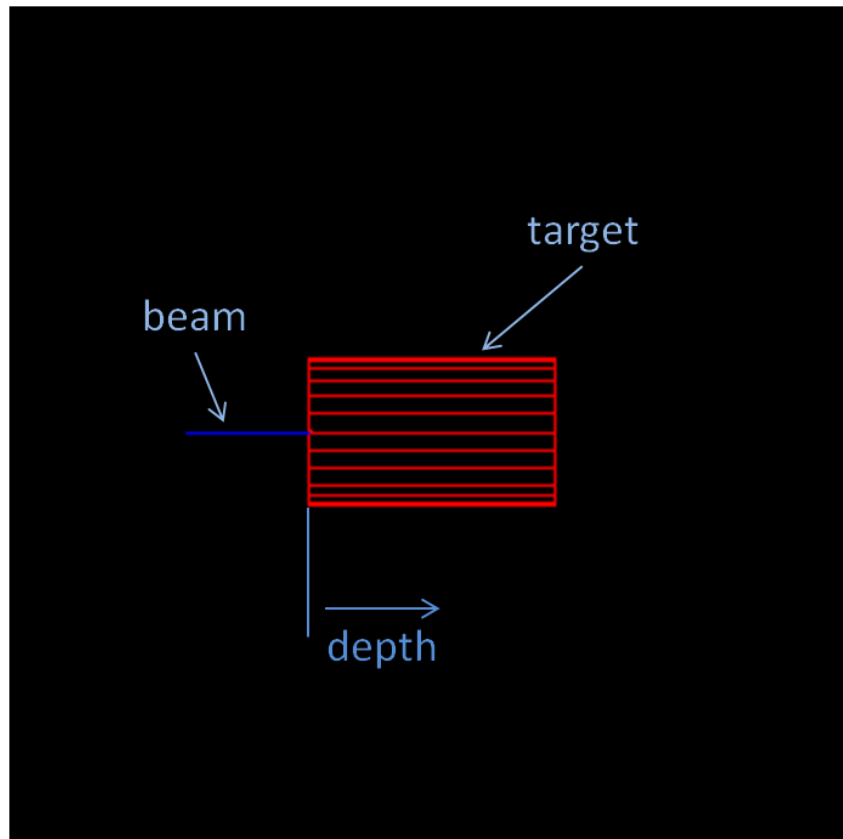


Figure 5.1: Simulation setup for measuring the Bragg peak depth.

Listing 5.1: Gate actor for measuring the depth dose distribution

```

/gate/actor/addActor DoseActor          BraggActor
/gate/actor/BraggActor/save             Output/Dose
/2400_MeV.txt
/gate/actor/BraggActor/attachTo         human
/gate/actor/BraggActor/stepHitType      random
/gate/actor/BraggActor/setVoxelSize 60. 60. 0.1 cm
/gate/actor/BraggActor/enableDose      true

```

5.1 Dose distribution in water

As water is often used as a model for human tissue, the simulation was first conducted using it as target material. 10^7 primary carbon ions were used in the following simulations.

Figure 5.2 shows a typical result of the deposited dose as a function of the depth for a few different primary energies. In this plot like in all other plots, which show a certain

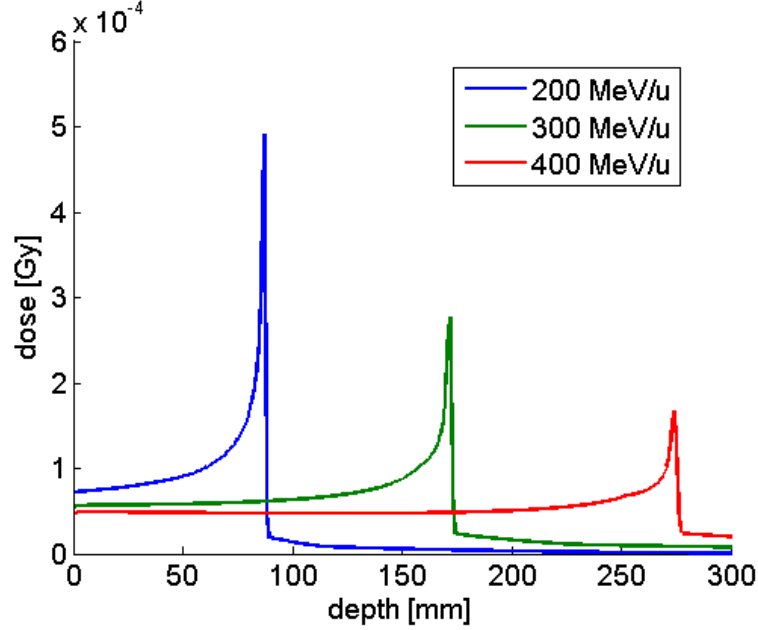


Figure 5.2: Depth-dose distribution for 10^7 carbon ions hitting a water target at 3 different energies.

value as a function of depth, the beam can be imagined hitting the target at a depth equal to 0, meaning that it is coming from the left hand side. The low entrance dose, the rise to the peak, the sharp decrease behind the Bragg peak and the dose tail can be seen (see also section 2.3.2). Furthermore one can see that the height of the peak decreases with increasing energy, meaning a lower dose for targets deeper in the body for the same number of primary ions. Additionally higher primary energies mean higher penetration depths.

5.2 Dose distribution in other materials

In order to get knowledge of other kinds of tissue, the target materials were changed in the simulation to lung, skull and brain tissue. The general form of the depth-dose distribution did not change, but the depth of the peak shifts, as can be seen in figure 5.3. All materials have rather similar entrance dose and peak heights but different penetration depths. The Bragg peak depths range from about 115 mm for skull to about 650 mm for lung tissue, with water and brain being located in their middle at 172 mm and 162 mm respectively.

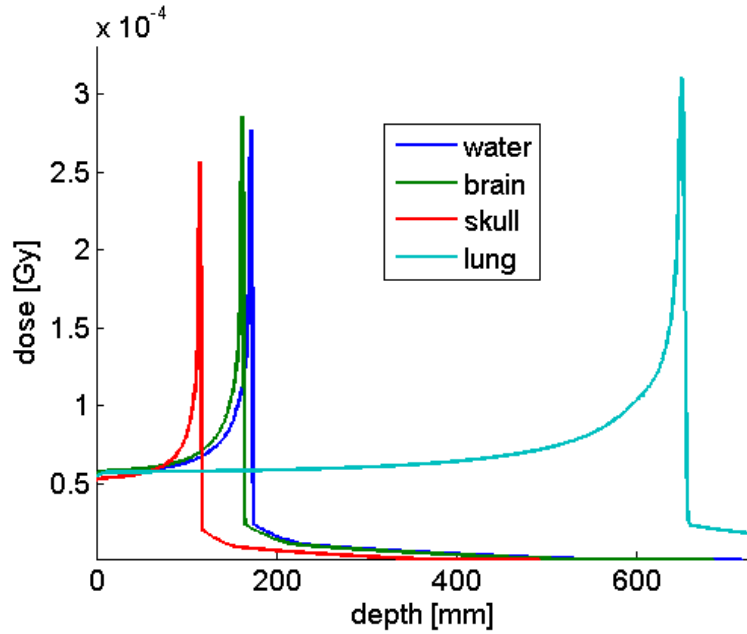


Figure 5.3: Depth-dose distribution for 10^7 carbon ions hitting different materials at 300 MeV/u.

Furthermore, the Bragg peak depth as a function of the energy for different materials was of interest. The results are shown in figure 5.4. As expected, the penetration depth increases with increasing primary ion energy.

5.3 Verficiation of simulations

The verification of the simulated data was also an important point. This was done with the help of some measured data and data from other simulation tools. The experimental data for water were taken from [15]. Again, the Bragg peak position was defined as the position of the maximum dose and 10^7 primary carbon ions were used for the simulations. The other simulation environment which was used to compare the Gate data to was SRIM (Stopping and Range of Ions in Matter), a software which calculates the range of ions in matter [16]. These data sets were compared to the results acquired by simulations using Gate and G4.water (see section 4). The results are shown in figure 5.5. The general agreement between the simulated and the measured data is relatively high. When one takes a closer look at the data points, it can be seen that the penetration depth simulated with Gate is lower than the experimental values and the values simulated with SRIM. In [15], other results were mentioned, which were acquired by different simulation tools (FLUKA, PHITS). These results also lie below the experimental values. To further

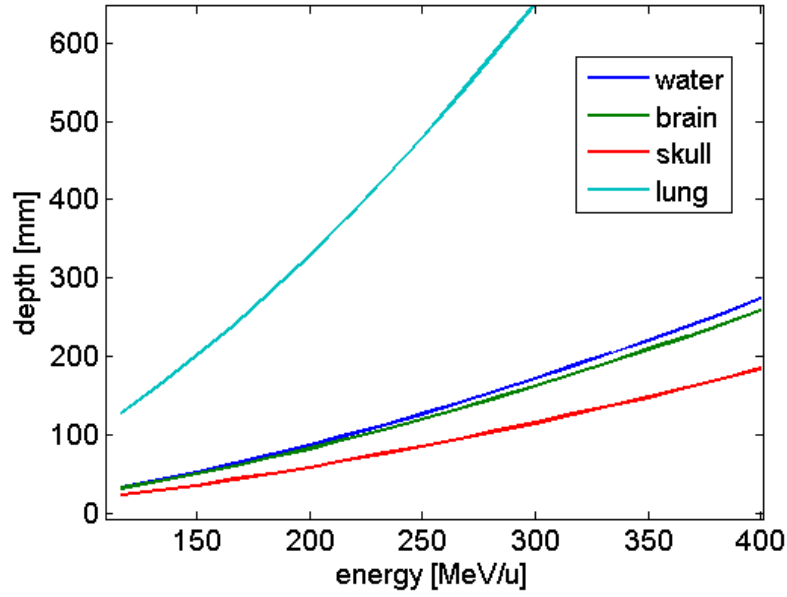


Figure 5.4: Depth of the Bragg peak for carbon ions with varying energy for different materials.

visualize this result, one can take a look at the relative error of the data simulated with Gate, when compared to a fit to the experimental data and to the SRIM data, respectively. These fits were obtained by a 2^{nd} order polynomial fit to these data sets with Matlab. The result is shown in figure 5.6. The Bragg peak depth is underestimated by 4 % at the maximum relative deviation when compared to the experimental data. This maximum deviation occurs at small primary energies.

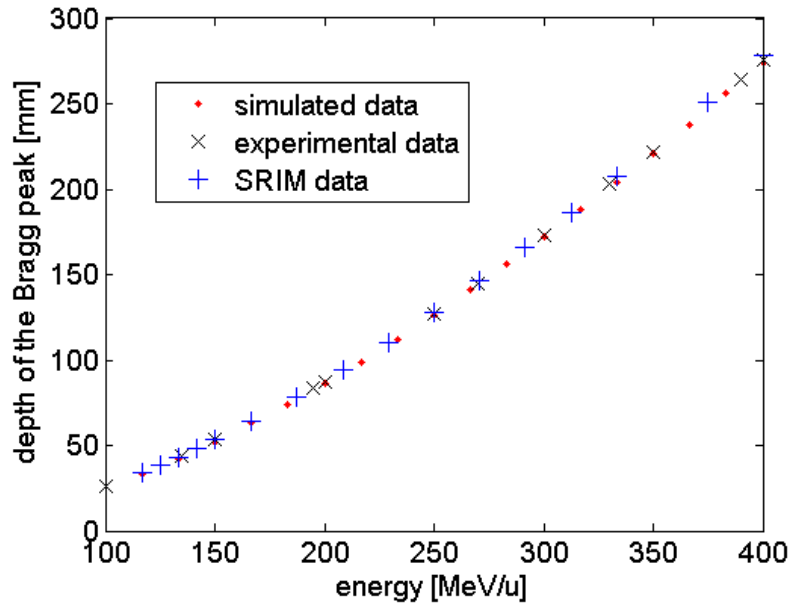


Figure 5.5: Comparison of simulated and experimental penetration depth of carbon ions in water.

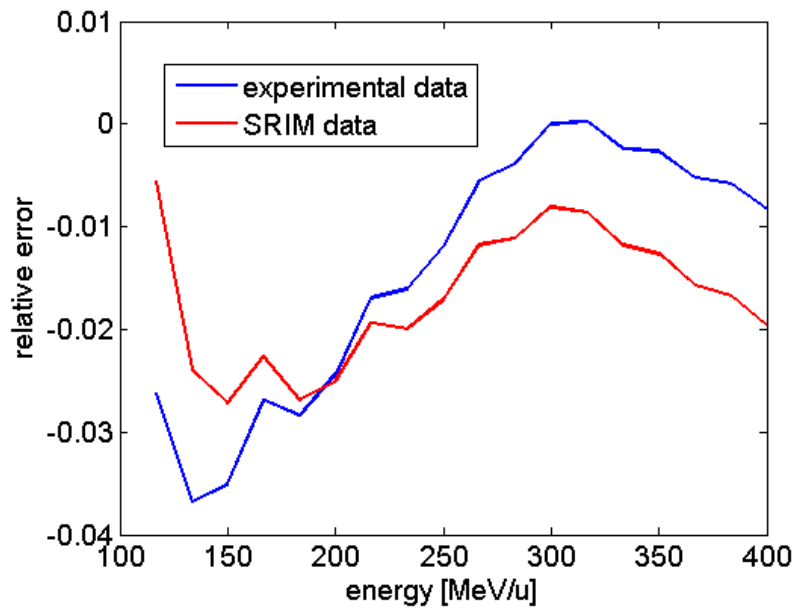


Figure 5.6: Relative error of the the simulated penetration depth of carbon ions in water when compared to different data.

6 Angular distribution

For the simulations described from now on a Gaussian shaped carbon ion beam with a standard deviation of 3 mm was used. It is also interesting to know about the angular distribution of the prompt photons emerging from the target, because it was of importance to check if there is a favourite direction of these photons. The outcome of the investigation of that problem should then be taken into account when thinking about building a detector for prompt gammas. If there was such a direction, it would probably be better to detect photons emerging in this direction, due to the higher count rate.

It is obvious that the results of these investigations strongly depend not only on the primary energy of the carbon ions and the target material, but also on the size and shape of the target, because of attenuation effects. For example, if the target would be smaller than the distance to the Bragg peak in the direction of the beam, all the photons which would have been produced at the Bragg peak are not produced and thus can not be detected. On the other hand, if a large target was investigated, absorption effects would be strong and reduce the amount of detected photons greatly. As a compromise, spherical targets with a radius equal to the Bragg peak depth were built. In this way it was ensured, that the Bragg peak was really inside the target, and that attenuation effects for photons originating from the peak are isotropic, because the distance between the peak and the outside of the target is the same in every direction. As a consequence of the considerations above, the size of the target varies with the primary energy, since the Bragg depth also depends on it (see also section 5).

For the following simulations, 10^7 primary carbon ions have been used. The geometry of the whole setup is shown in figure 6.1. In this plot the polar angle θ is described. It is 0° for the direction from the target to the source and 180° from the middle of the target in beam direction. The second angle for spherical coordinates, with which this setup is described, is the angle ϕ , which is shown in figure 6.2.

The detector for measuring the angular distribution of prompt photons consists of a spherical shell with a radius of 5 meters, which is divided into parts of constant $\Delta\theta$ and $\Delta\phi$. These spherical shell parts were, in the first simulations, connected to a so called *Kill*

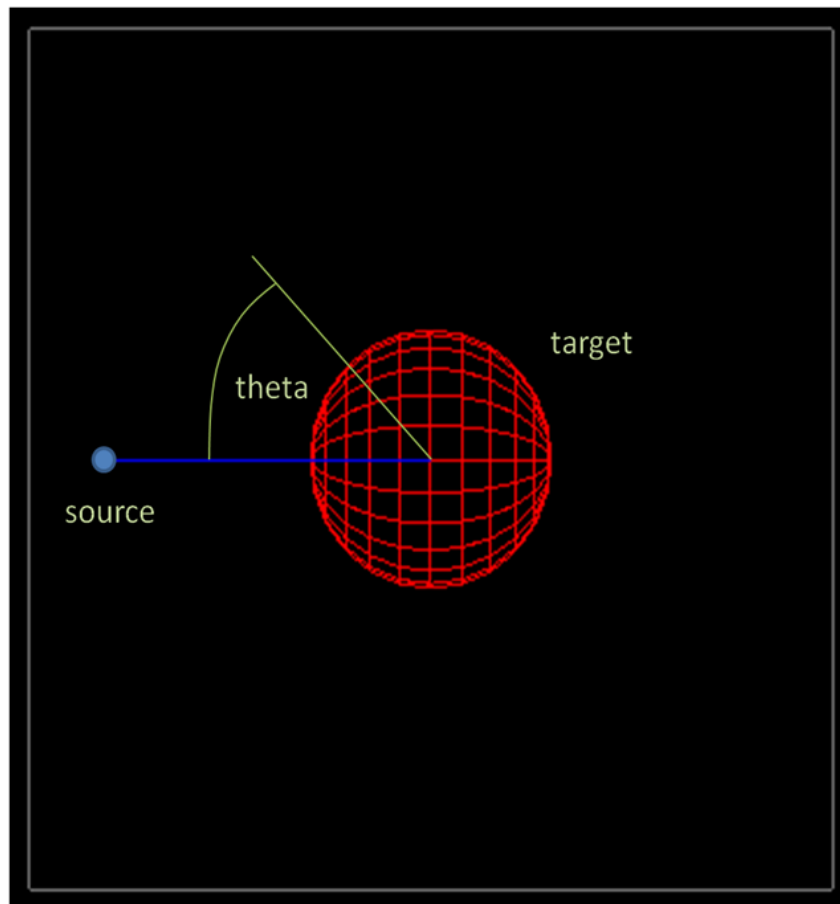


Figure 6.1: Geometry of the setup for measuring the angular distribution of prompt photons.

Actor (see also section 4). This *Kill Actor* kills (meaning extinguishes) all the photons passing through the volume it is connected with and counts the number of particles it killed. A typical code example for such an actor is shown in listing 6.1.

Listing 6.1: Gate code for building the detectors for measuring the emission angle of prompt photons

```
/gate/world/daughters/name Volume_15_40
/gate/world/daughters/insert sphere
/gate/Volume_15_40/setMaterial Vacuum
/gate/Volume_15_40/vis/setColor magenta
/gate/Volume_15_40/vis/forceWireframe
/gate/Volume_15_40/geometry/setRmax 500. cm
```

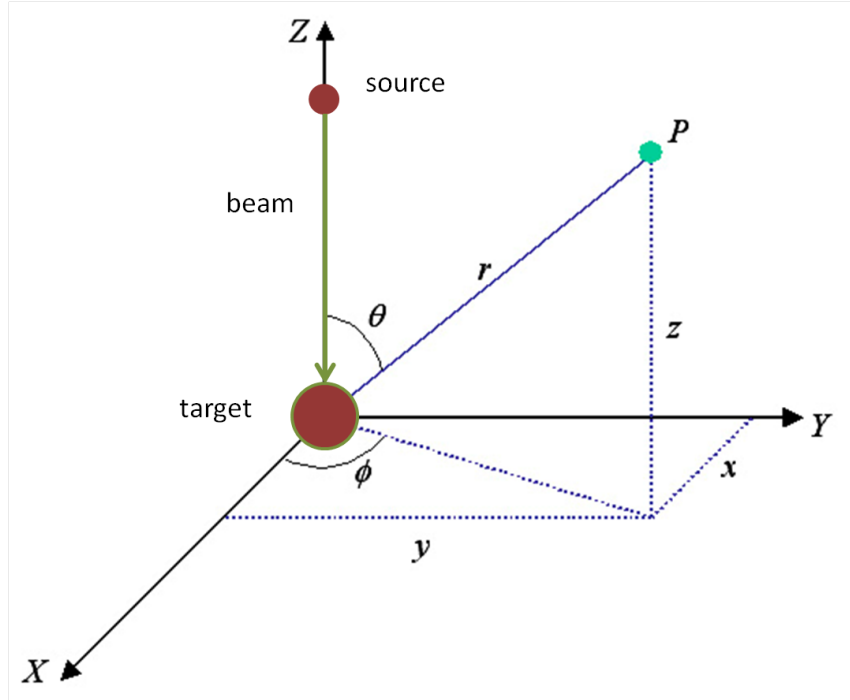


Figure 6.2: Full description of the coordinate system of the setup for measuring the angular distribution of prompt photons.

```
/gate/Volume_15_40/geometry/setRmin 499.5 cm
/gate/Volume_15_40/geometry/setPhiStart 30. deg
/gate/Volume_15_40/geometry/setDeltaPhi 20. deg
/gate/Volume_15_40/geometry/setThetaStart 10. deg
/gate/Volume_15_40/geometry/setDeltaTheta 10. deg

/gate/actor/addActor KillActor Killer_15_40
/gate/actor/Killer_15_40/save Output/3400MeV/
AngleOut_15_40.txt
/gate/actor/Killer_15_40/attachTo Volume_15_40
/gate/actor/Killer_15_40/addFilter particleFilter
/gate/actor/Killer_15_40/particleFilter/addParticle gamma
```

This actor measures all photons that are emitted in the region $\theta = 15 \pm 5$ and $\phi = 40 \pm 10$. With this resolution being valid for every detector, the whole sphere was divided 18 times in direction of θ and 18 times in the direction of ϕ , resulting in 324 detectors. The radius of the detector was chosen to be 5 meters, thus very much larger than the target, in order to really measure the emission angle and not to spoil this information by different

points of emission. The inner radius of this spherical shell was chosen to be 499.5 cm. A picture of the whole setup can be seen in figure 6.3. Each of the parts of the surface of the

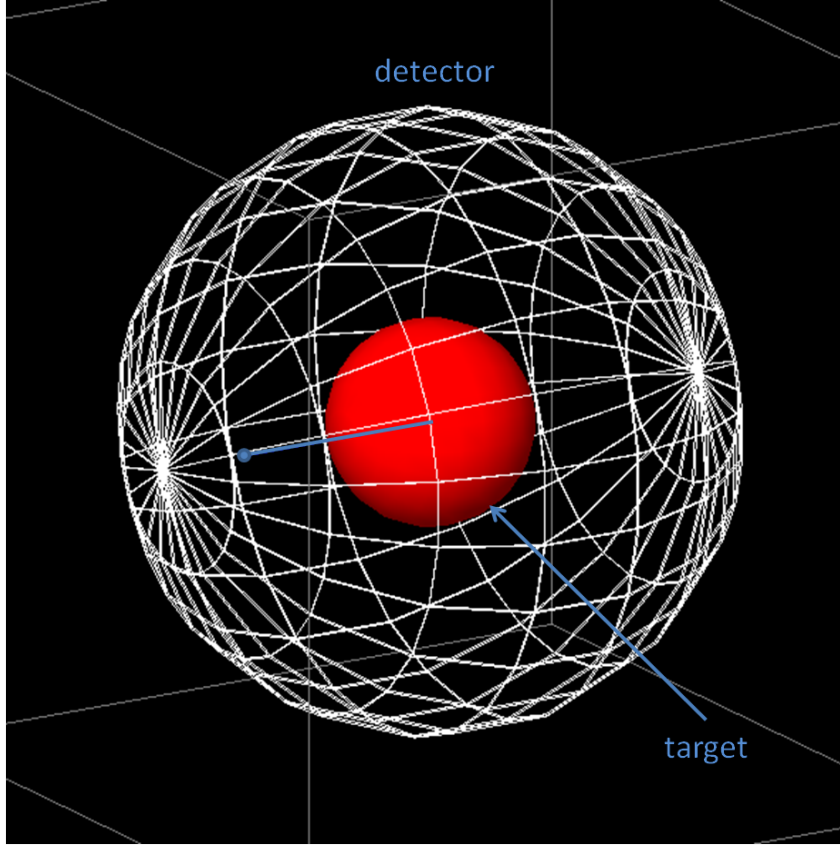


Figure 6.3: Simulation setup with detector for measuring the angular distribution of prompt photons (not true to scale).

spherical shell which is enclosed by white lines is one of the above mentioned volumes, to which a *Kill Actor* is attached.

6.1 Angular dependence

The simulation described above was first carried out for water at different primary ion energies. The results are shown in figures 6.4 - 6.6. These plots show the detected photons depending on the angle for different primary ion energies. These counts are normalised to the number of primary ions (10^7) and the solid angle the detector occupies. This is necessary because, as one can see from figure 6.3 for example, the covered solid angle depends on the angle θ . To get to the counts per steradian, the detected counts

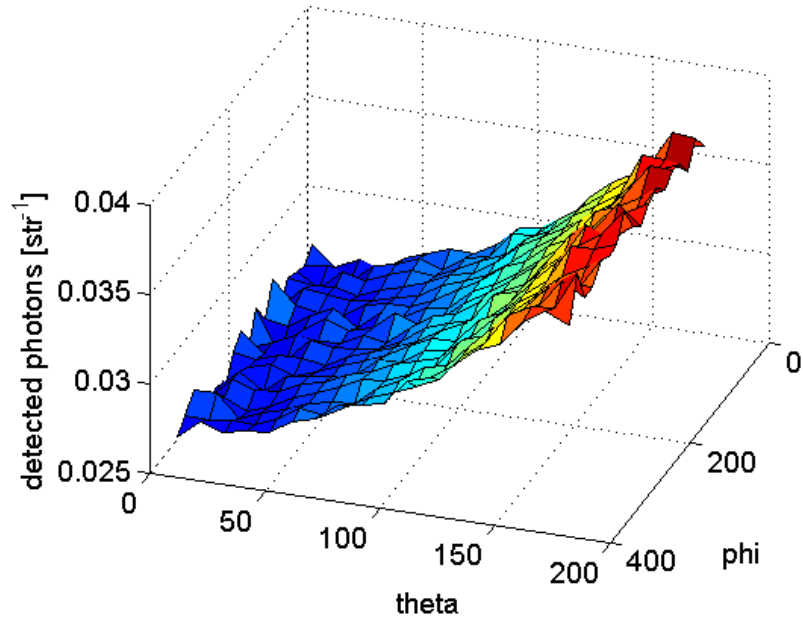


Figure 6.4: Angular distribution of prompt photons for carbon ions hitting a water target at 150 MeV/u.

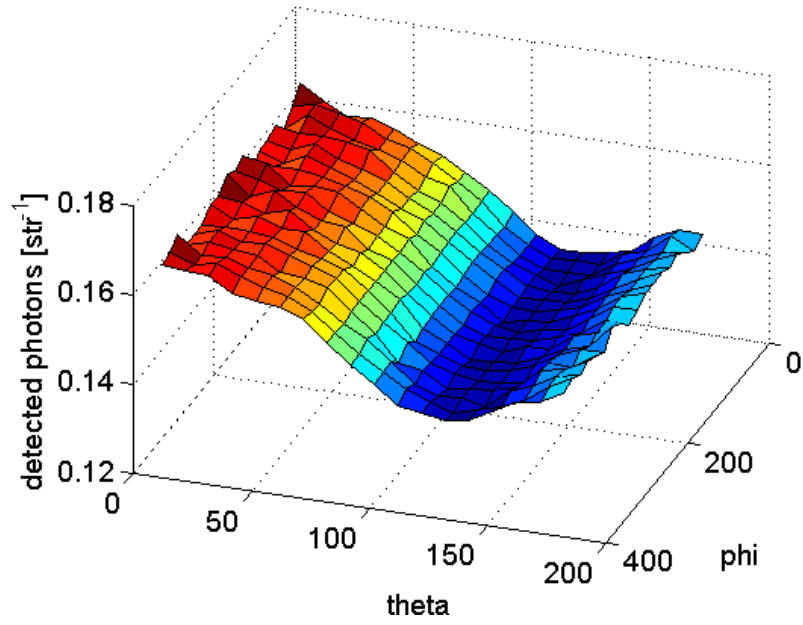


Figure 6.5: Angular distribution of prompt photons for carbon ions hitting a water target at 285 MeV/u.

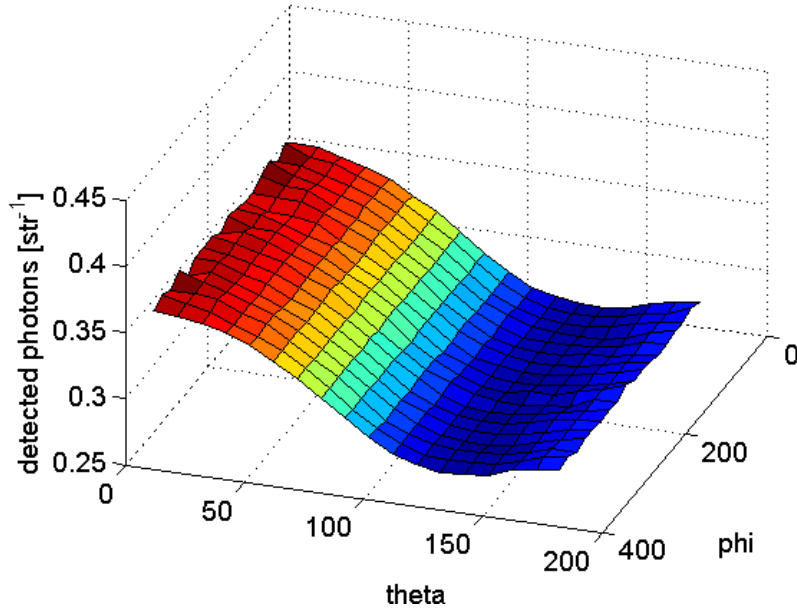


Figure 6.6: Angular distribution of prompt photons for carbon ions hitting a water target at 385 MeV/u.

were divided by a factor given in equation (6.1).

$$\frac{2 \pi (\cos \theta_1 - \cos \theta_2)}{18} \quad (6.1)$$

Here θ_1 and θ_2 are the 2 boundary angles of the detector. In this formula, the numerator equals the solid angle for all the 18 different detectors at the same angle θ . To get the solid angle of one detector, the division by 18 is necessary.

Several things can be seen in these plots. First, that the photon counts do not depend on the angle ϕ , except some fluctuations which can be attributed to low statistics, proving the expected isotropy in ϕ direction. Another thing is the change in the count rates. At 150 MeV/u about 0.035 photons are detected per steradian, whereas for 385 MeV/u about 0.35, 10 times as much, are counted. This effect can be explained by the fact, that the higher the primary ion energy the more energy these ions need to lose before they get stopped at the Bragg peak (which is inside of the target). In figure 6.7, one can see the overall detected photons for varying energy in water. Of course, these numbers would again be different for another shape of the target.

The most striking thing about the plots 6.4 - 6.6 is the change of the dependence on

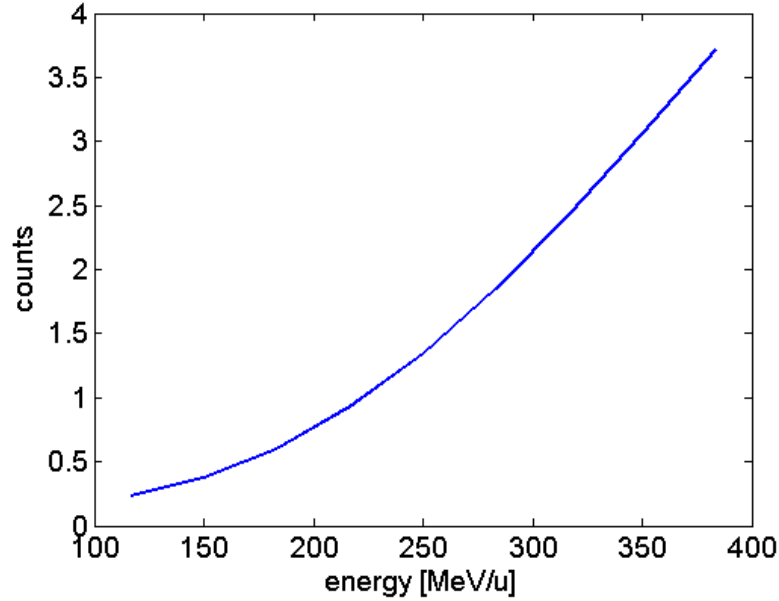


Figure 6.7: Detected photons per primary ion for carbon ions hitting a water target.

θ of the count rates with varying primary energy. For low primary ion energies, most photons are detected in beam direction. This would be an intuitive behaviour, as the preferred direction of the photon production is the beam direction, as can be seen in figure 6.8. For this plot, the photon production has been measured in a cone with an opening angle of 45° between the border of the cone and the central axis, along the 6 spatial axes ($x+$, $x-$, $y+$, $y-$ orthogonal to the beam; $z+$, $z-$ parallel to the beam) every millimeter. Furthermore, 10^7 primary particles have been used. The $z+$ direction is the beam direction, $z-$ is the opposite direction. One can see that after the Bragg peak, which is located at about 118 millimeter and is marked by a local maximum of the photon production, every direction has the same count rates. But in front of the peak, the count rates differ depending on the direction. All directions orthogonal to the beam have the same count rates (the line in the middle) in this area, but in beam direction, much more photons are produced than opposite to the beam direction. This kind of behaviour is found for every primary ion energy and for every photon energy range.

With this information, the dependence of the photon counts outside of the target for small energies can be explained. For these energies, the Bragg peak depth is quite small and as a consequence the target is small. For example, the Bragg depth for 150 MeV/u is about 52 mm in water. For this distance, absorption of photons does not play a major role for any of the important photon energies. As a consequence, most photons pass

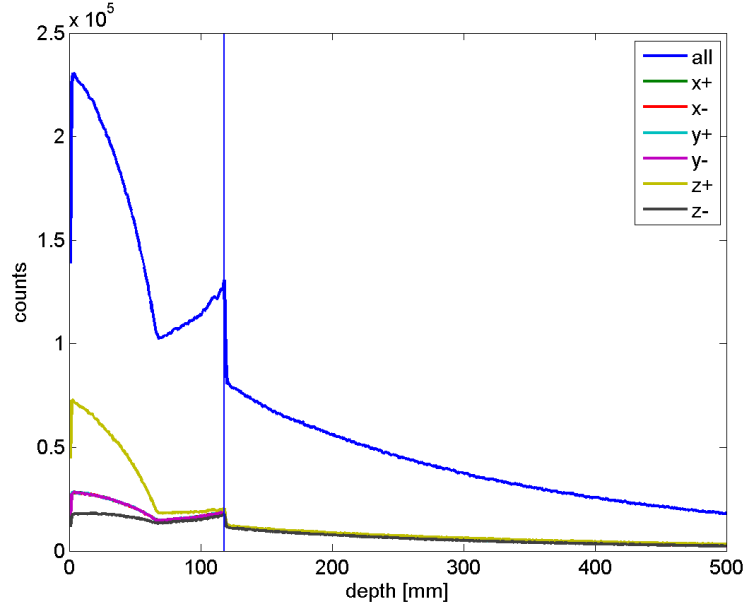


Figure 6.8: Angle dependent photon production for carbon ions impinging on a water target at 240 MeV/u (explanation see text). [17]

through the target and are detected, which leads to the maximum of the count rates in beam direction. To explain the shift of the maximum of the detected photons towards the opposite of the beam direction with increasing primary energy, one needs to take into account the photon energy, which is detailed in section 6.2.

6.1.1 Other materials

The same investigations have been made for other materials, namely for brain, skull and lung tissue, to see whether the same behaviour as for water can be found. The simulations yielded the results shown in figures 6.9 - 6.11. In these figures, the sum was formed over detectors with the same angle θ , because no dependence on the angle ϕ was observed in the previous investigation explained above, consequently it was not necessary to show it in the plots. The numbers are again normalised to a detector which occupies 1 steradian, and are taken per primary ion. This time, the sum over all detectors with the same angle theta was divided by a factor given in equation (6.2).

$$2 \pi (\cos \theta_1 - \cos \theta_2) \quad (6.2)$$

Here θ_1 and θ_2 are again the minimum and maximum angle of a detector. For lung tissue, the energies differ slightly from the other materials, because the penetration depth for

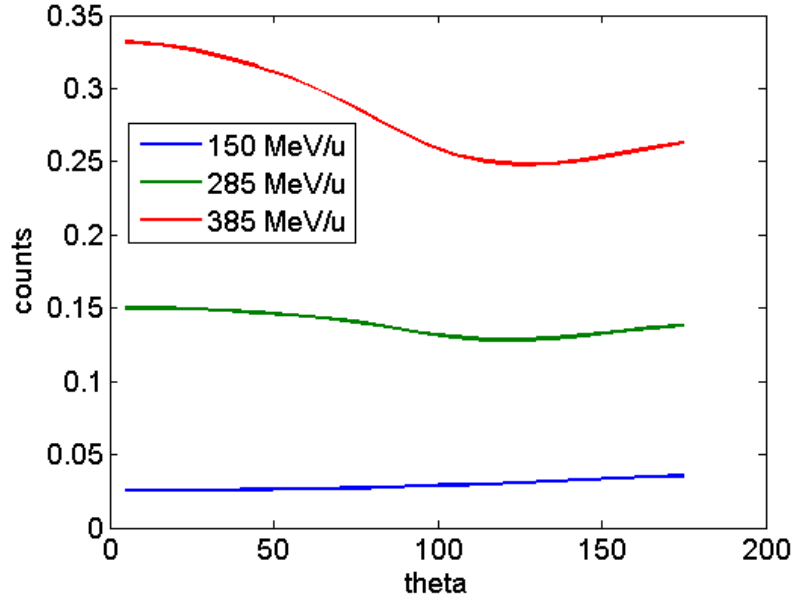


Figure 6.9: Angular distribution of prompt photons for 3 different carbon ion energies with a brain tissue target.

the same primary ion energies is much higher in lung tissue and simulations with higher energies than shown in plot 6.11 would result in unrealistically high penetration depths.

In plots 6.9 - 6.11, it can be seen that the behaviour with varying primary ion energy is the same for all materials. For low energies, the maximum of the counts is in beam direction, which can be explained by the maximum of the photon production in this direction for all primary energies. For higher energies, the maximum shifts in the direction of the source again. In figure 6.12 the total photon counts per primary ion for all the above mentioned materials can be seen. It is obvious, that the count rates do not differ much for different materials and the above mentioned simulation setup. The count rates are increasing with increasing primary ion energy. The counts are ranging from about 0.3 for the lowest simulated carbon ion energies to about 3.7 photons per primary ion for the highest energies.

6.2 Dependence on photon energy

Another important point that was to be addressed was whether there is a specific direction which is preferred by a specific photon energy. The reason for this was, that if it would turn out, that a special photon energy would be of higher interest because of a special spatial

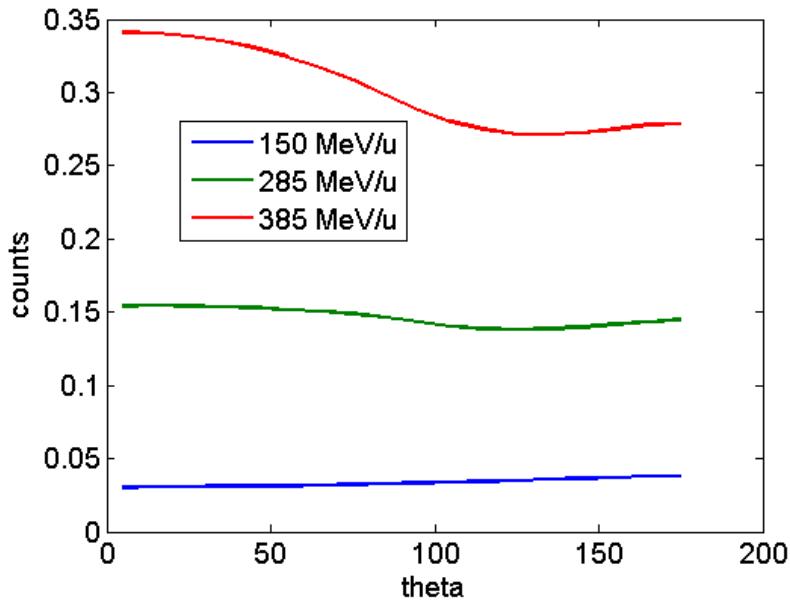


Figure 6.10: Angular distribution of prompt photons for 3 different carbon ion energies with a skull target.

production or some other yet unknown factors, one would know where it would be ideal to put a detector for this certain photon energy. For this purpose, the same simulation setup like in the simulations mentioned before was used, with one slight difference. Namely that the detecting actor in Gate was changed from a *Kill Actor* to an *Energy Spectrum Actor*. This actor records the energy of every particle of a certain kind, in the volume the actor is attached to (see also section 4). The result is an energy spectrum with an adjustable binning and adjustable minimum and maximum energy. A code example of one of these actors is given in listing 6.2. Additionally now always only one count number for one angle θ is shown in the following plots. This was done, because it was known from the above mentioned results, that the photon counts were evenly distributed in the angle ϕ . The detectors were again in 10° intervals with an average angle of $5^\circ, 15^\circ, 25^\circ, \dots$ etc.

Listing 6.2: Gate code for measuring the photon energy spectrum at a certain emission angle

```
/gate/world/daughters/name Volume_25
/gate/world/daughters/insert sphere
/gate/Volume_25/setMaterial Vacuum
/gate/Volume_25/vis/setColor magenta
```

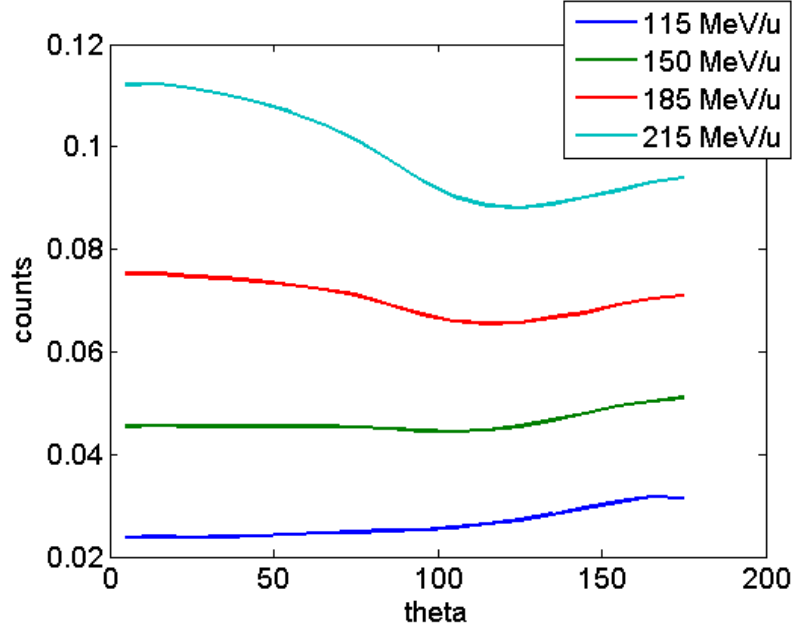


Figure 6.11: Angular distribution of prompt photons for 4 different carbon ion energies with a lung tissue target.

```

/gate/Volume_25/vis/forceWireframe
/gate/Volume_25/geometry/setRmax 500. cm
/gate/Volume_25/geometry/setRmin 499.5 cm
/gate/Volume_25/geometry/setThetaStart 20. deg
/gate/Volume_25/geometry/setDeltaTheta 10. deg

/gate/actor/addActor EnergySpectrumActor Speck_25
/gate/actor/Speck_25/save Output/SpecOut_25.root
/gate/actor/Speck_25/attachTo Volume_25
/gate/actor/Speck_25/energySpectrum/setEmin 0 eV
/gate/actor/Speck_25/energySpectrum/setEmax 15 MeV
/gate/actor/Speck_25/energySpectrum/setNumberOfBins 1500
/gate/actor/Speck_25/addFilter particleFilter
/gate/actor/Speck_25/particleFilter/addParticle gamma

```

In this code, the maximum of the recorded energy is set to 15 MeV, but the counts of the gammas with higher energy are stored in another bin, making sure that the information is not lost. The bin size is set to 10 keV. For the following plots, the sum was formed over a certain amount of these bins. For example to get the counts in the energy range from 0 - 2 MeV, the sum was formed over the first 200 bins. The results of these simulations

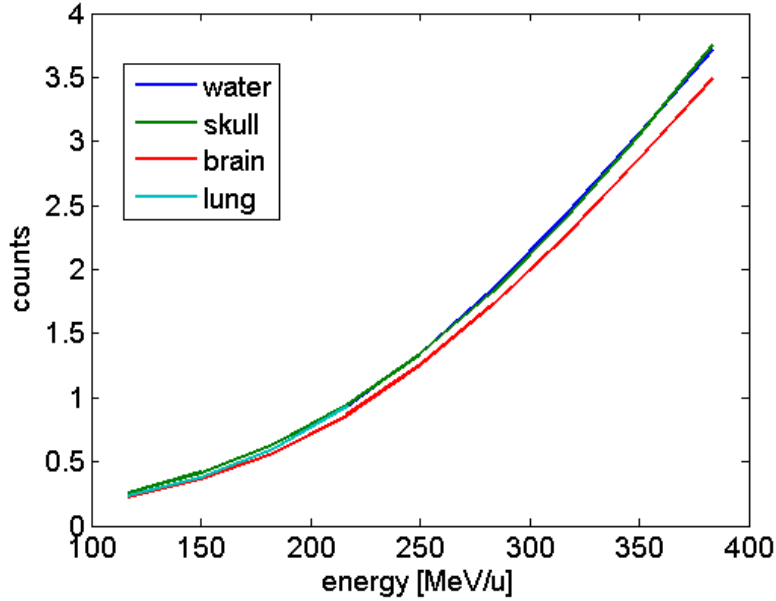


Figure 6.12: Total photon counts for carbon ions impinging on different materials as a function of the energy.

are shown in figure 6.13. Again, the counts in this plot were normalised to the solid angle of the detector and the number of primary ions. From results mentioned earlier (like in figure 6.5), it is known, that there is a maximum of photon detection in the direction opposite to the beam for higher primary ion energies. In figure 6.13 it can be seen that this behaviour can be attributed to the low energy photons. Only the photons below 2 MeV exhibit this behaviour. One can even take a closer look at this low energy range below 2 MeV, which is shown in figure 6.14. This behaviour can mainly be attributed to the gammas with an energy even below 0.5 MeV. This is valid for all primary ion energies. These particles are produced mainly in front of the Bragg peak, and their production is pictured in figure 6.15 (again 10^7 primary ions were used for this simulation).

For this low energy range, absorption is a relevant factor. As the primary energy increases, the target gets bigger in order for the Bragg peak to stay in its center. Along with that, the way for the particles, which are produced in the beginning of the target, gets longer when they are going in beam direction through the whole target, and absorption gets stronger. In the other direction (opposite to the beam direction), absorption is of course not so strong, because the way is much shorter. This effect is responsible for the decrease of low energy photon counts with increasing angle θ . Along with that, the total photon counts also decrease with increasing angle θ , because they consist to a large

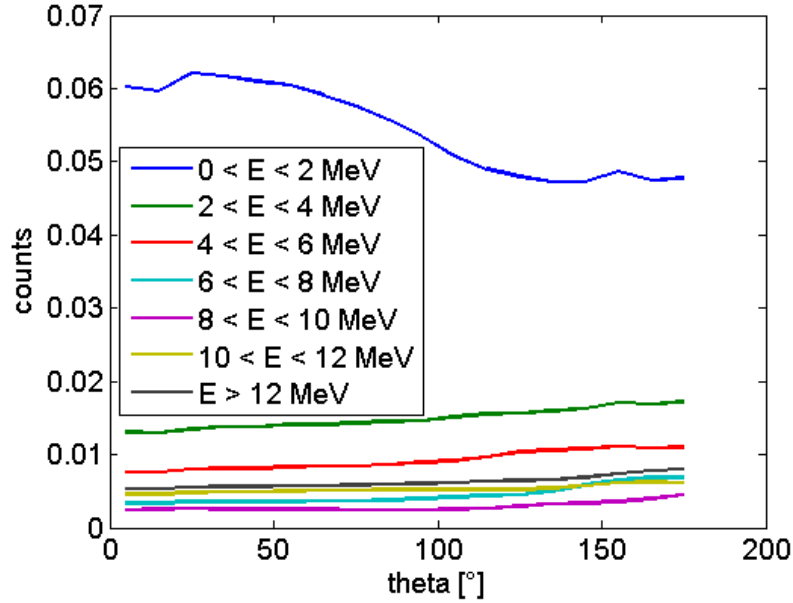


Figure 6.13: Angular distribution of detected photons for carbon ions impinging on a water target at 240 MeV/u for different photon energy ranges.

amount of low energy photons (see figure 6.13). For photons of higher energy, absorption is not so strong and in their preferred direction of production (in beam direction) a maximum of counts is detected outside of the phantom. A fact, which can be validated in figure 6.16. Additionally, the path through the target of photons with higher energy, which are produced in beam direction, is shorter than the one for lower energy photons, because they are produced to a large extent in the area of the Bragg peak, right in the middle of the target, as will be shown in section 7.3 for example. Consequently absorption is lower for these photons, because of their shorter path and their lower attenuation coefficient (see for example [17]). Similar results were obtained for other primary ion energies in water.

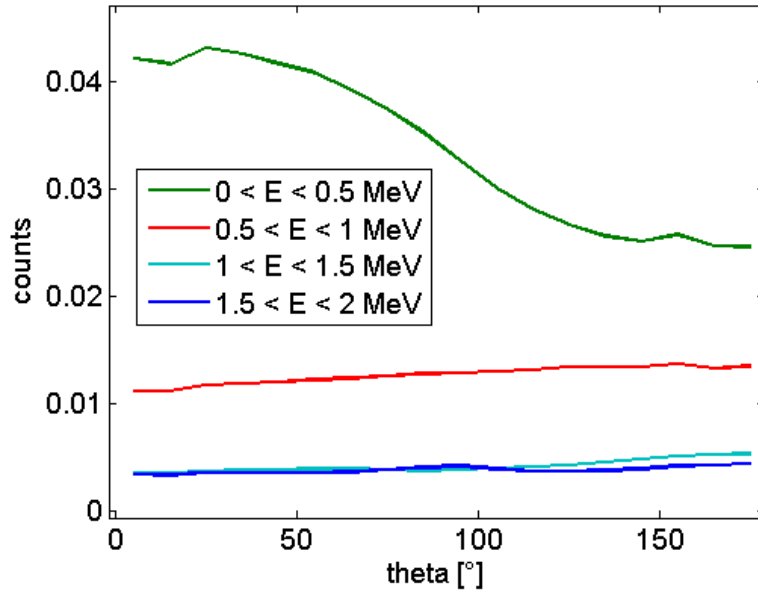


Figure 6.14: Angular distribution of different low photon energy ranges for carbon ions impinging on a water target at 240 MeV/u.

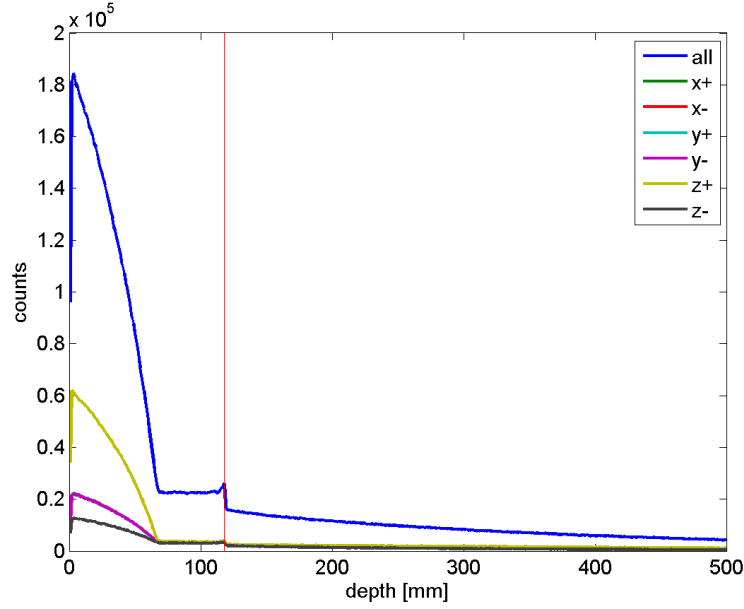


Figure 6.15: Angular dependence of the photon production for carbon ions impinging on a water target at 240 MeV/u for photons in the energy range from 0 - 0.5 MeV [17].

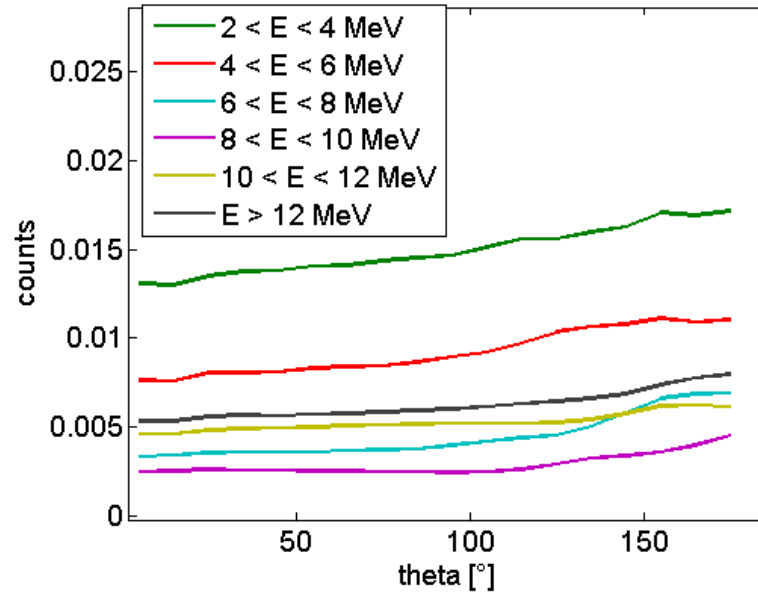


Figure 6.16: Angular distribution of different high photon energy ranges for carbon ions impinging on a water target at 240 MeV/u

7 Detection of the Bragg peak

7.1 Without collimators

As mentioned earlier, one of the main goals of this work was to determine the position of the Bragg peak on the inside of a target only by detecting the prompt gamma photons produced by the impact of the carbon ions during radiation therapy. Two different strategies were investigated to reach this goal. These two strategies differed from each other in the use of a collimator. For the first one, no collimator was used, whereas for the second one, a collimator was added to the setup. The setup with collimators is described in two chapters, where the first one can be seen as an introduction to the second one.

The first simulation setup is shown in figure 7.1. Again, the beam hits the target from the left hand side. The target is cylindrical with a radius of 30 cm and a length of 50 cm, and it has the colour red in this plot. In this and all following simulations, the target consists of water. Around the target, many small cylindrical volumes were built, which are all shown in white in the plot and which consist of vacuum. In the plot, only 5 of these volumes are shown for clarity reasons. Furthermore there was no gap in between the volumes in the simulations, it is nevertheless shown here so the volumes can be distinguished. All of these volumes are shells of cylinders, with a radius of 50 cm and a thickness of 10^{-7} m normal to the beam. The detector was built so thin in order to avoid double counted photons in 2 detectors next to each other. Furthermore, their length in beam direction is 1 mm. The first volume starts in beam direction right above the beginning of the target. Then, after 1 mm, the second volume follows without space in between them and so on. To each of these volumes, an *Energy Spectrum Actor* was attached, which records the energy spectrum of the photons passing through this volume. An example for the Gate code for one of these volume/actor combinations is given in listing 7.1.

Listing 7.1: Gate code for measuring the position and the energy of prompt photons.

```
/gate/world/daughters/name SpecVolume_0  
/gate/world/daughters/insert cylinder  
/gate/SpecVolume_0/setMaterial Vacuum
```

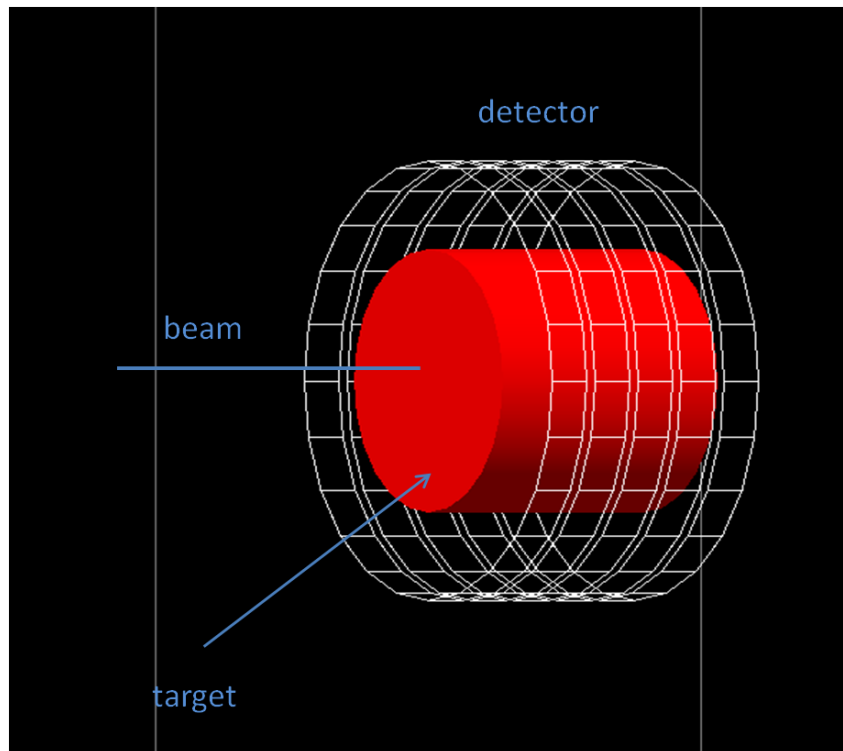


Figure 7.1: First simulation setup without collimators for measuring the Bragg peak.

```
/gate/SpecVolume_0/vis/setColor white
/gate/SpecVolume_0/vis/forceWireframe
/gate/SpecVolume_0/geometry/setRmax 50.00001 cm
/gate/SpecVolume_0/geometry/setRmin 50. cm
/gate/SpecVolume_0/geometry/setHeight 1. mm
/gate/SpecVolume_0/placement/setTranslation 0. 0. -0.5 mm

/gate/actor/addActor EnergySpectrumActor Speck_0
/gate/actor/Speck_0/save Output/Spektren/0mm/Spektrum.root
/gate/actor/Speck_0/attachTo SpecVolume_0
/gate/actor/Speck_0/energySpectrum/setEmin 0 eV
/gate/actor/Speck_0/energySpectrum/setEmax 15 MeV
/gate/actor/Speck_0/energySpectrum/setNumberOfBins 1500
/gate/actor/Speck_0/addFilter particleFilter
/gate/actor/Speck_0/particleFilter/addParticle gamma
```

In this listing, the first volume which begins right above the target is built. Again, the *Energy Spectrum Actor* records all the photons from 0 to 15 MeV. With this setup, the Bragg peak should be determined by counting the photons passing through the detectors. For most photon energy ranges, the photon production has a maximum at the Bragg peak and thus the detectors above this region should count more photons than detectors further away from it. With this information, it should be possible to calculate the Bragg peak.

The result of this simulation is shown in figure 7.2. The red dots in this plot indicate the photons detected on the outside of the phantom in the energy range from 2.3 - 6 MeV per primary ion. The black line indicates the scaled photon production at the same primary carbon ion energy in the same photon energy range. The photon production was divided by a factor, so its counts are similar to the detected photons, so both can be shown in one picture. This specific energy range was used for this and for future plots for reasons explained in [17]. One of them was already mentioned, namely the high absorption of lower energy photons. This, and the circumstance that these photons are rather produced in the beginning of the phantom and not at the Bragg peak and thus not contributing to the photon signal from the Bragg peak, are reasons for neglecting them. For further discussion of this issue, like justifying the upper energy limit, see [17].

What was expected to be seen in this plot was a pronounced peak of the detected photons right above the Bragg peak, from which it would be possible to directly calculate or see the place of the maximum of the photon production. But when looking at the picture, it

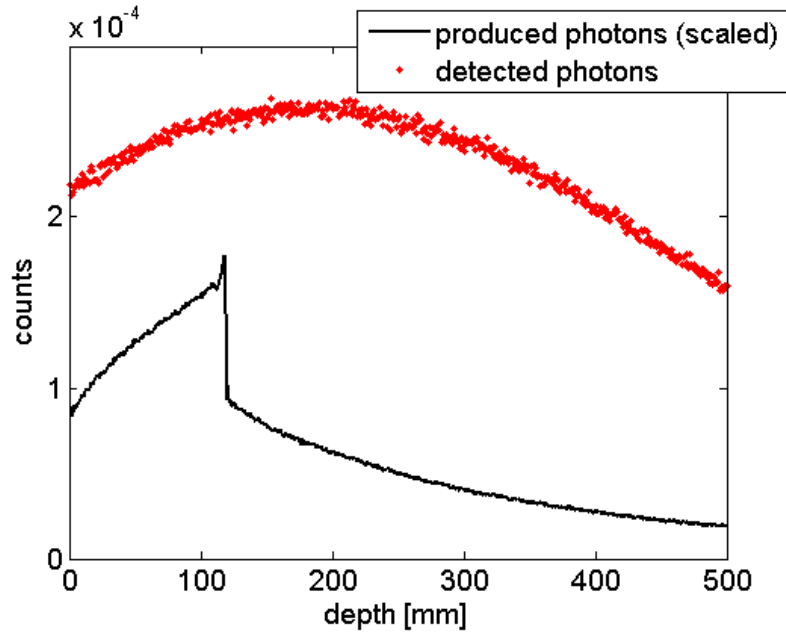


Figure 7.2: Scaled photon production and photon detection in the energy range from 2.3 - 6 MeV for carbon ions impinging on a water target at 240 MeV/u for a setup without collimators.

is obvious that this is not the case. The detected photons on the outside do not exhibit any kind of real peak in the area of the Bragg peak. The counts do increase slightly with increasing depth until about 200 mm, but the information about where the maximum of the photon production is, is lost. Or, in other words, the peak of the photon detection is too far away from the peak of the photon production to somehow link them. One reason for this shift of the peak of the photon detection in beam direction relative to the peak of the photon production is probably, that the photon production is not isotropic, but has a preferred direction in beam direction. More photons in front of and on the Bragg peak are produced in beam direction, as was already mentioned before for another energy range, but is true for every energy range. This causes these photons to hit the detector further in beam direction than their position of production was and the maximum of the detection to be shifted in beam direction relative to the maximum of the production. Although serious effort was made, it was not possible to connect the information from the detection to the information about the production in a satisfying way for several primary ion energies. Consequently a different detector setup had to be built for calculating the Bragg peak by detecting prompt gammas.

7.2 Ideal collimators

In the section above the problem of the shifting of the Bragg peak when detected with the mentioned simulation setup was discussed. The problem with this setup was, that many photons are produced in beam direction and hit the detector on the outside further in beam direction than their position of production was. The same problem also exists for photons being produced in backwards direction, hitting the detector far behind their place of production, but to a lesser extent. To avoid this problem, collimators were added to the simulation setup. By doing this it should be achieved, that only the photons produced at the same depth in beam direction as the detector from which they are detected are counted. The changed setup is shown in figure 7.3. The collimators are shown in green.

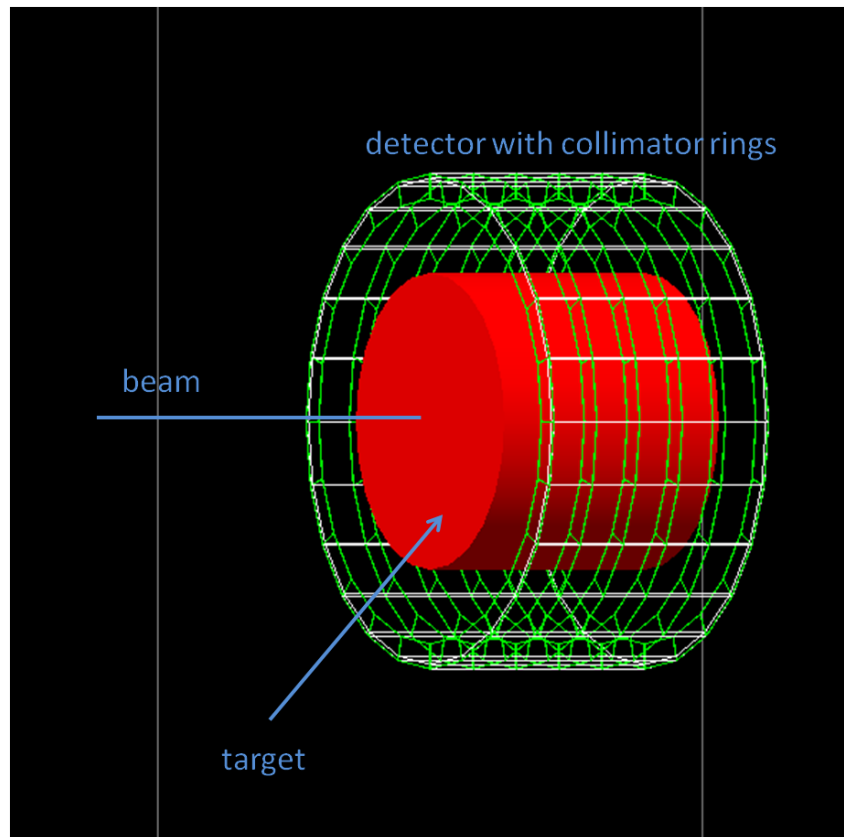


Figure 7.3: Simulation setup for the detection of the Bragg peak with collimators.

In the real simulation, far more collimators were built with much less space in between them. For clarity reasons, only a few of them are shown here. They have the form of a hollow cylinder with a very small height of the cylinder and an inner radius of 47 cm and an outer radius of 50 cm. These collimators should avoid the problem of the shift of

the Bragg peak due to oblique photons hitting the detector, meaning photons travelling a long way in or opposite to the beam direction before hitting the detector. These photons should be extinguished by the collimator and thus not be detected. A Gate code example of a part of this setup is given in listing 7.2.

Listing 7.2: Gate code for building the setup for measuring the Bragg peak using ideal collimators.

```
/gate/world/daughters/name collimator_0
/gate/world/daughters/insert cylinder
/gate/collimator_0/setMaterial Vacuum
/gate/collimator_0/vis/setColor magenta
/gate/collimator_0/vis/forceWireframe
/gate/collimator_0/geometry/setRmax 50. cm
/gate/collimator_0/geometry/setRmin 47. cm
/gate/collimator_0/geometry/setHeight 0.0001 mm
/gate/collimator_0/placement/setTranslation 0. 0. -0. mm

/gate/actor/addActor KillActor Killer_0
/gate/actor/Killer_0/attachTo collimator_0
/gate/actor/Killer_0/addFilter particleFilter
/gate/actor/Killer_0/particleFilter/addParticle gamma

/gate/world/daughters/name SpecVolume_0
/gate/world/daughters/insert cylinder
/gate/SpecVolume_0/setMaterial Vacuum
/gate/SpecVolume_0/vis/setColor red
/gate/SpecVolume_0/vis/forceWireframe
/gate/SpecVolume_0/geometry/setRmax 50.00001 cm
/gate/SpecVolume_0/geometry/setRmin 50. cm
/gate/SpecVolume_0/geometry/setHeight 1. mm
/gate/SpecVolume_0/placement/setTranslation 0. 0. -0.5 mm

/gate/actor/addActor EnergySpectrumActor Speck_0
/gate/actor/Speck_0/save Output/Spektren/0mm/Spektrum.root
/gate/actor/Speck_0/attachTo SpecVolume_0
/gate/actor/Speck_0/energySpectrum/setEmin 0 eV
/gate/actor/Speck_0/energySpectrum/setEmax 15 MeV
```

```
/gate/actor/Speck_0/energySpectrum/setNumberOfBins 1500  
/gate/actor/Speck_0/addFilter particleFilter  
/gate/actor/Speck_0/particleFilter/addParticle gamma
```

The first paragraph of this code builds the volume for the collimator with a length (the dimension of the collimator orthogonal to the beam direction will from now on be referred to as length of the collimator) of 3 cm and a thickness (the dimension of the collimator in beam direction will from now on be referred to as thickness of the collimator) of 10^{-7} m. The second paragraph attaches a *Kill Actor* to this volume. A *Kill Actor* extinguishes every particle of a given kind (photons in this case) and counts them (see also section 4). This is also the reason for building the collimator that thin, because it makes no difference for the *Kill Actor*. The 3rd and the 4th paragraph build the detector, which is located at the end of the collimator at 50 cm radius. This detector again records the spectrum of the photons passing through it and it also has the shape of a hollow cylinder, with a height of the cylinder of 1 mm and a difference between inner and outer radius of 10^{-7} m. This construction is followed in beam direction by another collimator and another detector, so that one detector is always between 2 collimators. This construction is repeated over the whole length of the phantom. Of course, this is not a realistic setup, because in reality there is no such thing as a perfect collimator, which the *Kill Actor* represents, but it is good to test the principle of this kind of detection method.

The results for this simulation, which was once again conducted for water at several primary ion energies, are shown in figure 7.4. In the figure, the red dots represent the detected photons in the energy range from 2.3 to 6 MeV as a function of the distance to the beginning of the target at a carbon ion energy of 240 MeV/u. Furthermore the black line represents the scaled photon production in the same photon energy range. It is obvious that the maximum of the photon detection is still not right above the peak of the photon production. It is shifted slightly opposite to the beam direction. But the general shape of the counts on the outside as a function of the depth is now closer to the photon production, compared to the simulation setup without collimators. It rises from the beginning until the region of the peak and falls off sharply afterwards .

But still it is not possible to calculate directly to the depth of the Bragg peak from the photons detected outside without further considerations, which was the goal of these investigations. To do this the finite length of the collimator has to be taken into account, which is the main reason for the shift of the Bragg peak.

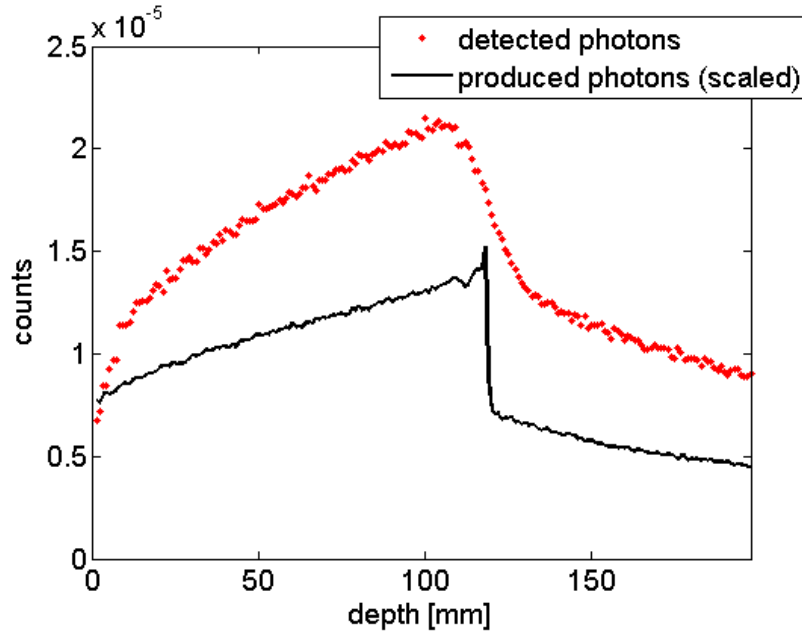


Figure 7.4: Photon counts for setup with ideal collimators in the energy range from 2.3 - 6 MeV for carbon ions impinging on a water target at 240 MeV/u.

7.2.1 Calculation of the response function

To calculate which effect the finite collimator length has on the outcome of the simulation, it is instructive to take a look at figure 7.5. In this plot, the ion beam is displayed by the black horizontal line on the lower side of the picture. r is the radius of the detector, c is the collimator length and d is the width of the detector. The whole construction on the upper side of this plot is a detector with one collimator on each side. The point “0” is the point right under this detector and the point X is some point at a distance x from this point. Now the probability for a photon produced in X to hit the detector right above the point “0” needs to be calculated. For this derivation, some simplifications have to be made. First, it is assumed that the photon production is isotropic. This is not entirely true, as can be seen from figure 6.8, for example. Second, it is assumed that all photons are produced right in the line of the beam. This is also not the case in reality, as the beam itself has a certain width and moreover, the beam spreads laterally when propagating through air and through the target. An effect, which was for example described in [2].

The probability for a photon produced in X to hit the detector above “0” is simply (under the assumptions taken above and neglecting effects in the water target for now) the solid angle the detector occupies as seen from X , divided by 4π . The solid angle of

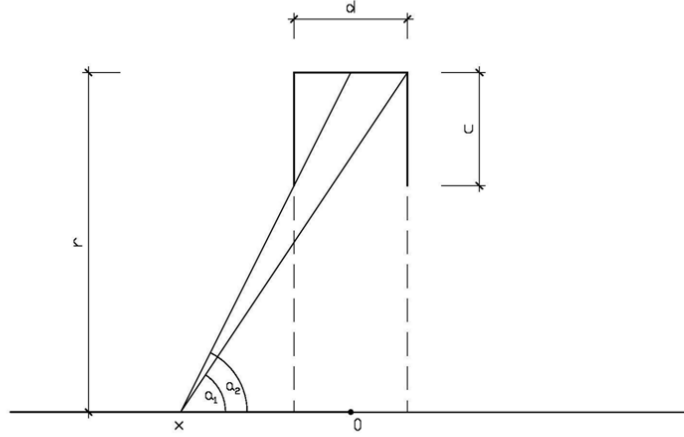


Figure 7.5: Schematic picture of the simulation setup for measuring the Bragg peak position by detecting prompt photons (explanation see text).

the detector is calculated by taking the part of the surface of the unit sphere around X , which is cut out of it by the angles α_1 and α_2 . The first thing that needs to be done is to calculate these angles from the geometry. From figure 7.5 it can be seen that this can be done as in equation (7.1) and equation (7.2).

$$\tan(\alpha_1) = \frac{r}{x + \frac{d}{2}} \quad (7.1)$$

$$\tan(\alpha_2) = \frac{r - c}{x - \frac{d}{2}} \quad (7.2)$$

To get the mentioned surface part of the unit sphere an integration has to be performed over the whole solid angle the detector occupies in spherical coordinates, like they were described in figure 6.2, with α replacing θ . This integral is shown in equation (7.3).

$$I = \int_{\alpha_1}^{\alpha_2} \sin(\alpha) d\alpha d\phi \quad (7.3)$$

In this equation ϕ represents the azimuthal angle of the coordinate system, and the integration over ϕ yields 2π . Combining equations (7.1), (7.2) and (7.3) yields equation (7.4).

$$I = -2\pi \cos(\alpha) \Big|_{\alpha_1}^{\alpha_2} \quad (7.4)$$

$$\alpha_1 = \arctan\left(\frac{r}{x + \frac{d}{2}}\right) \quad (7.5)$$

$$\alpha_2 = \arctan\left(\frac{r-c}{x-\frac{d}{2}}\right) \quad (7.6)$$

When evaluating these equations, the probability p , for a photon hitting the detector in the absolute distance x from its origin, can be calculated as in equation (7.7).

$$p = \frac{1}{2} \left(\frac{1}{\sqrt{\left(\frac{r}{x+d/2}\right)^2 + 1}} - \frac{1}{\sqrt{\left(\frac{r-c}{x-d/2}\right)^2 + 1}} \right) \quad (7.7)$$

To get to this probability, the integral I which defines the solid angle the detector occupies has been divided by 4π and equations (7.5) and (7.6) have been inserted in equation (7.4). This probability distribution is shown in figure 7.6. The probability for a point in the

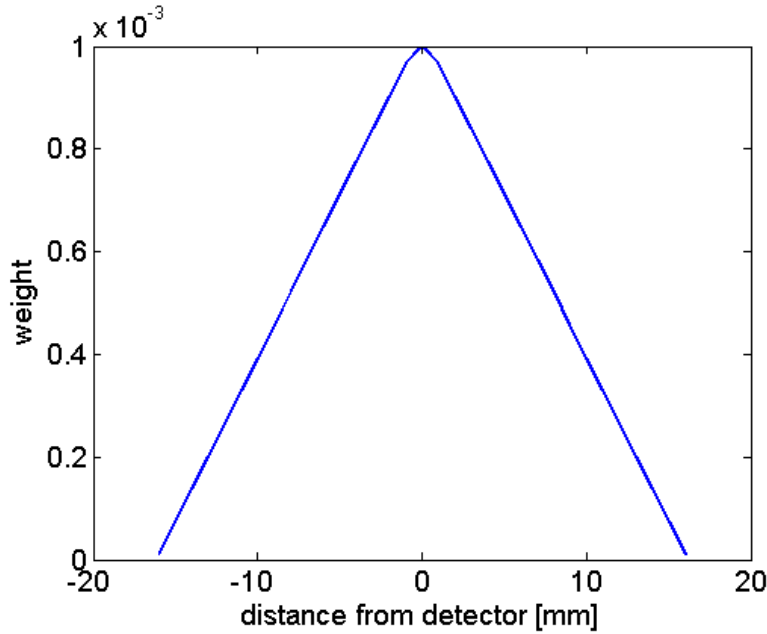


Figure 7.6: Probability distribution for a photon originating in the beam to hit the detector as a function of the distance from the detector for a certain collimator geometry.

beam with $x \geq 16$ mm to emit a photon in the detector is (when neglecting scattering as it was done during the whole derivation) equal to zero for a setup with a collimator length of 3 cm a detector width of 1 mm and a detector radius of 50 cm, for which this function was calculated in this picture. Also the point of the highest probability is right under the detector. This function will from now on be called convolution function or (detector) response function.

With this knowledge, the produced photons can be linked to the detected photons and vice versa. This is done with the help of a convolution. A convolution is a mathematical operation on 2 functions which produces a 3rd function, which can be seen as a modified version of one of the 2 original functions. A convolution is in Matlab, where all the calculations were performed, defined as in equation (7.8).

$$w(k) = \sum_j u(j) v(k - j + 1) \quad (7.8)$$

In this case, the function $v(i)$ is the probability distribution for a photon to be detected a distance x away from the place of production, which was calculated in equation (7.7). And the function $u(i)$ is the photon production inside of the target. To get the photons detected in one point of the detector, the photons produced in an arbitrary point of the target have to be taken and multiplied by the probability that a photon from this point is detected in this certain detector, and sum this up over all the points in the target. This is exactly what a convolution does. The function $w(k)$ should consequently be a good approximation for the photons detected on the outside of the phantom.

The results of this approach are shown in figure 7.7. The counts in this picture are again per primary ion. The blue line represents the convolution of the photon production and the derived response function. The red dots are the photons detected on the outside and the black line is the scaled photon production. It is obvious that the shape of the convolution and the detected photons are quite similar, but the counts are much higher for the convolution. This can be attributed to absorption and scattering in the water target. To prove this, the same simulation was started again, this time without the photoelectric effect, the Compton effect and gamma conversion. This can be achieved by turning these effects off in the physics list in the Gate simulation. The result of this simulation is shown in figure 7.8. It is obvious that the detected photons and the convolution fit almost perfectly. Consequently, the response function is a viable strategy for linking the produced and the detected photons. Another detail which has to be added here is the fact, that not the whole photon production was used for the convolution, but a photon production consisting of the same production density as there is in the area spanned by the angles $\alpha = 88 - 92$. This was done, because these are the angles contributing directly to the detected photons. At angles smaller or larger than these, the photons would hit the collimator and thus would not be detected, or only if they were scattered (but scattering was turned off in this simulation, consequently this was not possible). As the photon production is close to isotropic, this does not change much. The difference is shown in figure 7.9. To get to the numbers of the photon production orthogonal to the beam, the

actual count rates for these angles were taken and multiplied by a factor which scaled them up to the full solid angle of 4π . Numerically, this factor was about $\frac{4\pi}{0.4386}$, where 0.4386 is the solid angle these angles occupy. In figure 7.9, it can be seen that in front of the Bragg peak, the count rates orthogonal to the beam are a bit lower than the average count rates, meaning that the production rate is a bit lower in this direction than the average production rate.

7.2.2 Calculation of the Bragg peak

In the previous chapter, the calculation from the photon production to the photon detection has been discussed. But the goal of this work was to calculate the other way around, from the photon detection to the photon production and with that, to the depth of the Bragg peak. The first approach to achieve this goal was to simply reverse the above mentioned process of the convolution of the photon production with the response function. This was done by the means of the deconvolution of the detected photons with the response function. This should yield the photon production on the inside of the target. Unfortunately it turned out that this process is too sensitive to noise in the signal of the detected photons. Consequently, it was not possible to reconstruct the photon production by means of deconvolution.

The starting point for another possible way was to make a model of the photon production, which depends on a few parameters. The photon production in the energy range from 2.3 - 6 MeV was modelled as 2 straight lines, 1 in front of and 1 after the Bragg peak, with a jump discontinuity in between them. This model of the photon production depends on 5 parameters: the gradient and the offset of the 2 straight lines, representing 4 independently selectable parameters. The 5th and most important of all is the position of the Bragg peak, where the first line ends and the second one begins. In figure 7.10, the photon production and the model function with 5 guessed parameters is shown. The parameters were chosen wrong on purpose. For example the Bragg peak depth was chosen to be 100 mm, which is much too low as the real depth is about 118 mm.

As a next step, this model function had to be convoluted with the discussed response function. But first the response function had to be adjusted slightly, because of scattering and absorption losses. As can be seen from figures 7.7 and 7.8, absorption losses in the water target (radius = 30 cm) reduce the photon counts on the outside to nearly exactly half of what would be expected without these losses. This fact is introduced to the response function by dividing it by 2. This factor ensures, that the photon production convoluted with the response function yields the detected photons. This issue will be discussed more

thoroughly in section 7.3.

All the following calculations have been carried out using the Matlab function `nlinfit`, which does an iterative least squares fit of model parameters defining a model function when compared to a given “true” function. Now the model function for the photon production is convoluted with the newly adapted response function. The convolution of these 2 functions representing the model function for the photon detection, which is used as the function `nlinfit` compares the detected photons to (the detected photons representing the “true” function). If the sum of the squares of the differences in each point of these 2 functions is higher than a certain adjustable threshold, the parameters of the model function for the photon production are changed and the convolution and comparison is started again. This is done as long as either the sum of the squares of the differences is under the threshold or the maximum of iterative steps is reached. This process is pictured in figure 7.11. The output of this Matlab function are the 5 parameters of the model function, for which the convolution with the response function is closest to the detected photons. The result of such a fit is shown in figure 7.12. The fit is close to the photon production. The Matlab function `nlinfit` calculates not only the parameters of the model function, but also confidence intervals for them. The result for the Bragg peak depth for this fit was 118.2 ± 0.4 mm at a 95 % confidence level, which is very accurate. Similar calculations have been made for other primary ion energies, which proved that this strategy is also feasible for them. The results are shown in table 7.1 again with 95 % confidence intervals. The reason for the deviation of the calculated Bragg peak depth from the true value will

energy [MeV/u]	fitted Bragg depth [mm]	true Bragg depth [mm]
120	37.3 ± 0.2	35
240	118.2 ± 0.4	118
400	263.1 ± 2	274

Table 7.1: Calculated and true Bragg peak depths for carbon ions impinging on a water target at several primary ion energies.

be discussed in the next chapter. In figure 7.13 the convolution of the initially guessed and the finally fitted model function for the photon production with the response function and the actually detected photons can be seen. The photons detected on the outside of the target have been used to calculate the Bragg peak position inside of the water target with the help of a detector response function for an ideal simulation setup with *Kill Actors* working as collimators.

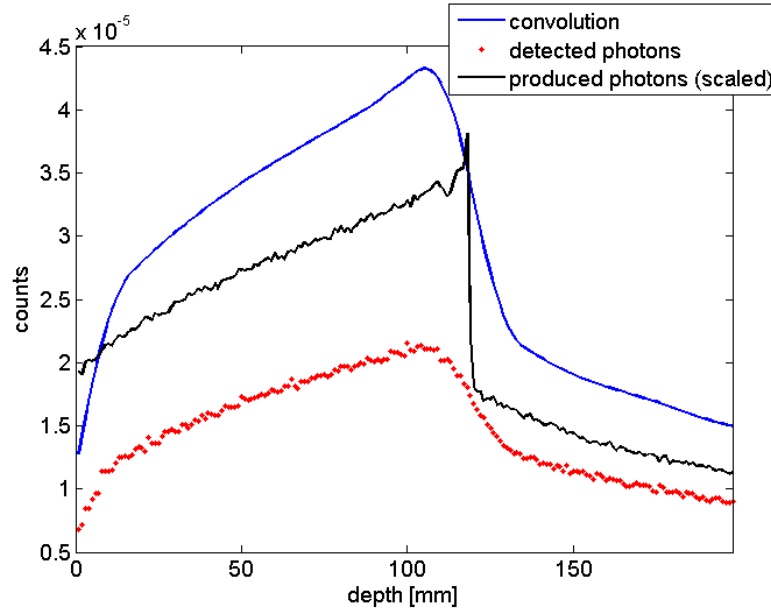


Figure 7.7: Detected photons compared to the convolution in an energy range from 2.3-6 MeV for carbon ions impinging on a water target at 240 MeV/u for a setup with ideal collimators.

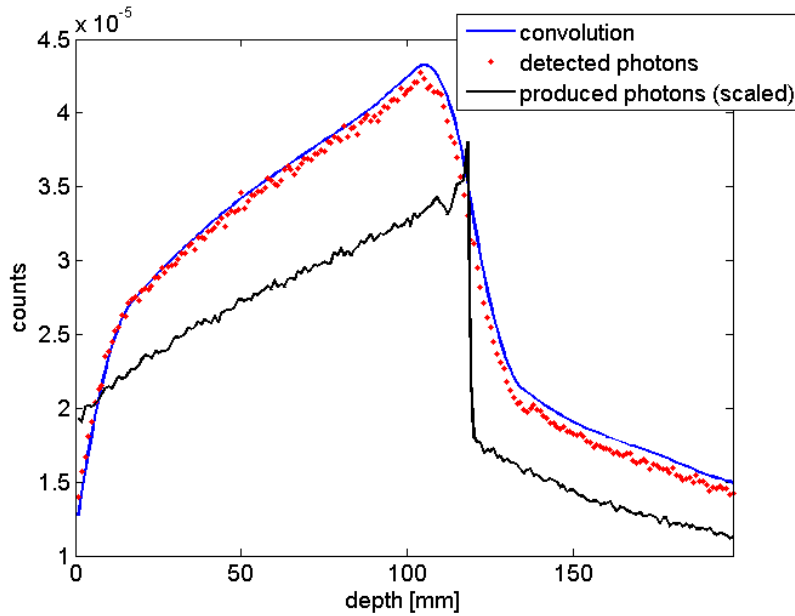


Figure 7.8: Detected photons compared to the convolution in an energy range from 2.3 - 6 MeV without photon scattering for carbon ions impinging on a water target at 240 MeV/u for a setup with ideal collimators.

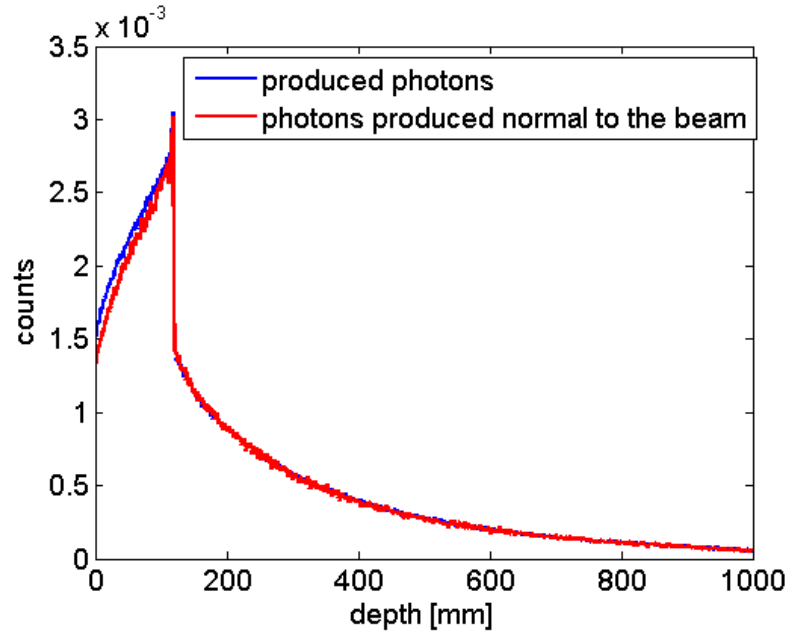


Figure 7.9: Photon production in the energy range from 2.3 - 6 MeV orthogonal to the beam (scaled) and in 4π for carbon ions impinging on a water target at 240 MeV/u (data received from BSc. Dominik Steinschaden).

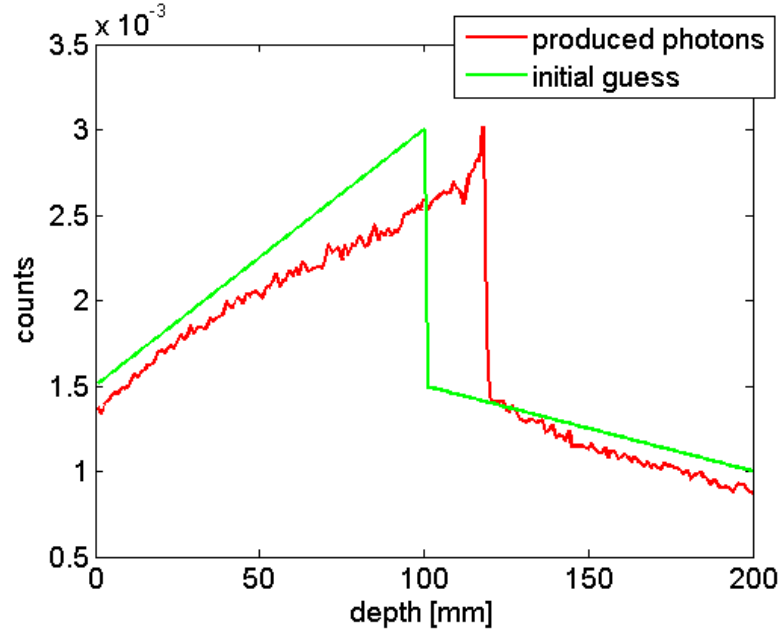


Figure 7.10: Photon production for carbon ions impinging on a water target at 240 MeV/u in the energy range from 2.3 - 6 MeV and model function for the same energy range with guessed parameters.

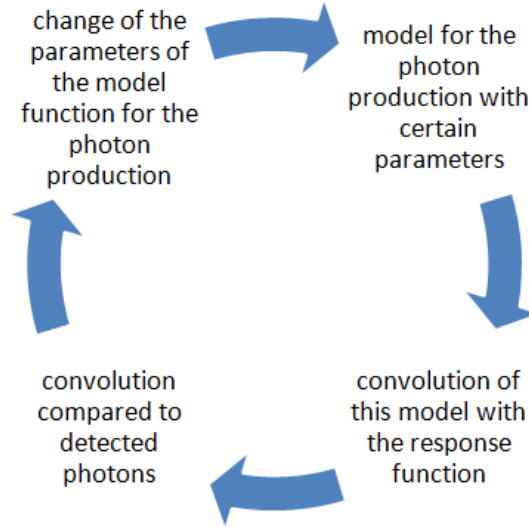


Figure 7.11: Fitting process for the model of the photon production.

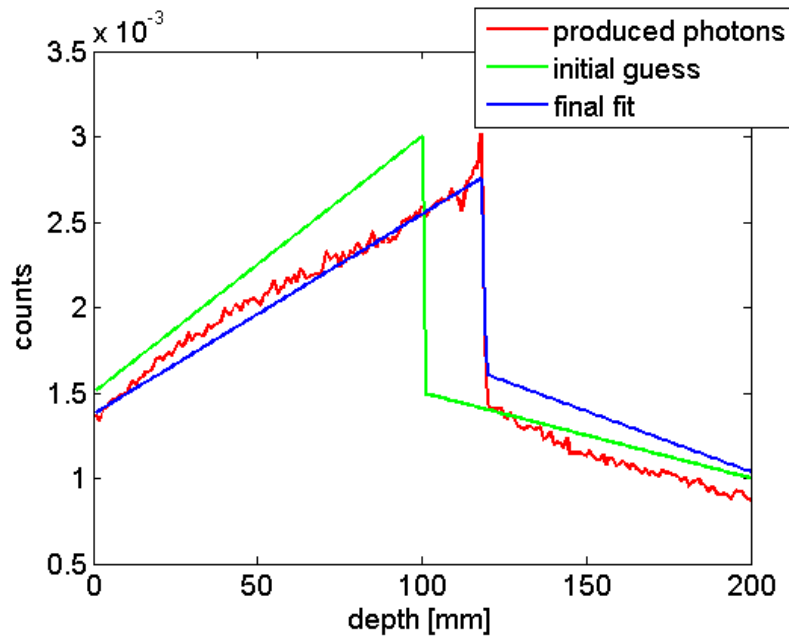


Figure 7.12: Photon production in an energy range from 2.3 - 6 MeV for 240 MeV/u carbon ions impinging on a water target with guessed and fitted model function for a setup with ideal collimators.

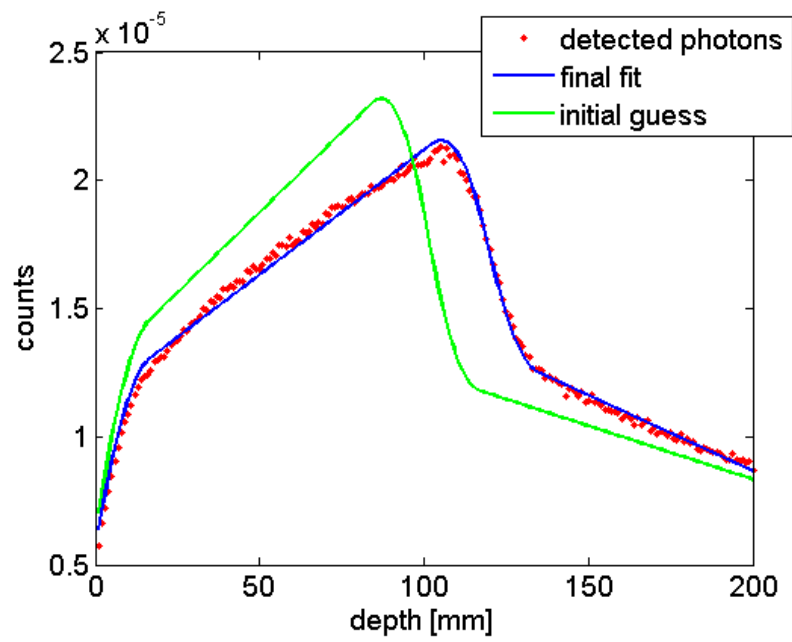


Figure 7.13: Convolution and detected photons for the energy range from 2.3 - 6 MeV for carbon ions impinging on a water target at 240 MeV/u for a setup with ideal collimators.

7.3 Realistic collimators

The simulation setup in the previous section was of course idealized and was only built to prove that the principle of the link between the photon production and the photon detection via the response function is working. This principle had been proven. The setup was not realistic because there is no such thing as a perfect collimator in reality. The *Kill Actors* acting as collimators in the previous simulations were exactly such a non existing perfect collimator. For the setup to become more realistic, the collimators were changed from *Kill Actors* to lead collimators. A plot of the setup is shown in figure 7.14. This time, the green rings are made of lead. Apart from that the setup is

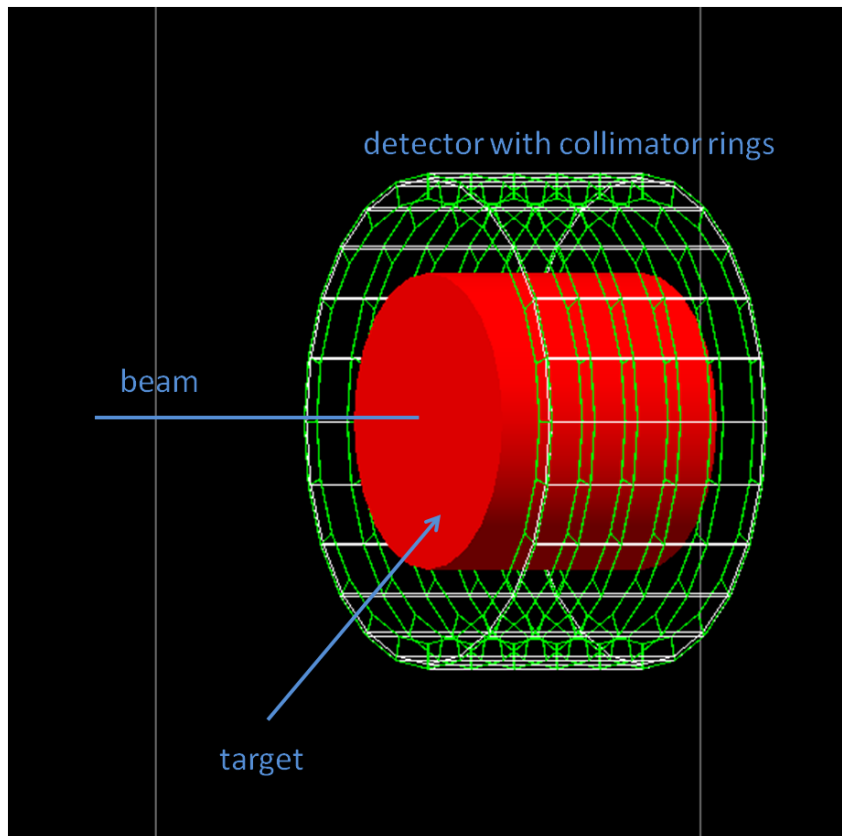


Figure 7.14: Simulation setup for measuring the Bragg peak by detecting prompt photons with lead collimators.

identical to the one previously used. Again, the number of collimators was drastically reduced in the plot for clarity reasons. In the course of the simulations, the exact dimensions of the collimators, like the space in between them, their thickness and their length were changed to get optimal results. The geometry is shown in more detail in figure 7.15.

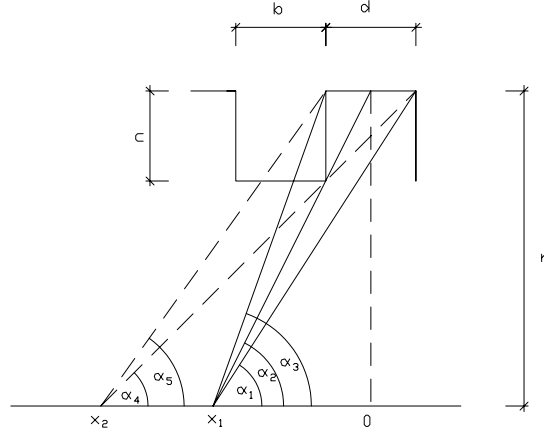


Figure 7.15: Geometry of the simulation for measuring the Bragg peak by detecting prompt photons setup as seen from the side (explanation see text).

In the text, the length marked with c will be referred to as collimator length, the length marked with b will be referred to as collimator thickness. With this geometry, the same simulations as in the previous part were conducted. Namely carbon ions with varying energy were shot at a water cylinder with a radius of 30 cm and a length of 50 cm and the resulting photons in the energy range from 2.3 - 6 MeV were detected on the outside with the goal of calculating the Bragg peak. When trying to link produced and detected photons as was done previously, the changed collimators have to be taken into account, which leads to a changed response function. The changed response function will again be derived under two assumptions. First, that all the photons are produced right in the axis of the target, in the line of the beam. Second, that the photon production is isotropic.

7.3.1 Calculation of the response function

For the new response function, the penetration of the collimators had to be taken into account. The new response function consists of the previously derived response function (for ideal collimators) plus 2 additional terms, which take into account the mentioned septal penetration (penetration of the lead collimators). The general strategy for calculating the additional terms of the response function is to calculate the probability for a photon produced a distance x from the detector to be emitted in the right direction (towards

the detector) and multiply it with the probability that this photon also penetrates the collimator. This probability is exactly the response function at a point X from the origin. The probability of the photon being emitted in the right direction is calculated analogue to section 7.2, with the new geometry being shown in figure 7.15.

The first additional term is added for the points x_1 , which are the ones still having a direct view of the detector (of course for these points, the previously derived response function is still valid and has to be added to this term). For these points, the photons need to be emitted between the angles α_2 and α_3 , for hitting the detector after penetrating through the collimator. These angles are calculated in equations (7.9) and (7.10).

$$\tan(\alpha_2) = \frac{r - c}{x_1 - \frac{d}{2}} \quad (7.9)$$

$$\tan(\alpha_3) = \frac{r}{x_1 - \frac{d}{2}} \quad (7.10)$$

The probability, that a photon is emitted between these 2 angles is calculated analogue to section 7.2. The result is given in equation (7.11) for absolute values x_1 .

$$p = \frac{1}{2} \left(\frac{1}{\sqrt{\left(\frac{r-c}{x_1-d/2}\right)^2 + 1}} - \frac{1}{\sqrt{\left(\frac{r}{x_1-d/2}\right)^2 + 1}} \right) \quad (7.11)$$

The probability for a photon emitted between these 2 angles to penetrate the collimator and consequently get into the detector needs to be calculated. For this purpose, the mean angle needs to be computed, which is defined in equation (7.12).

$$\alpha_{\text{mean}} = \frac{\alpha_2 + \alpha_3}{2} \quad (7.12)$$

An estimation was formed then, namely that photons travel a distance t through the collimator, which is given in equation (7.13).

$$t = \frac{c}{\sin(\alpha_{\text{mean}})} \frac{b}{b + d} \quad (7.13)$$

The first part of this equation represents the whole distance the photon travels from the point where it is exactly the distance c away from the nearest detector to hitting the detector when travelling in a angle α_{mean} to the beam. The second term in the equation comes from the fact that not the whole distance is travelled through lead, but also through the spaces in between the collimators. These gaps consist of vacuum. Thus the

distance travelled through lead, which the t stands for, is reduced by the fraction of the collimator thickness b divided by the collimator thickness plus the thickness of the gap of the detector d (for visualization see also figure 7.15).

The probability for a photon to pass through the collimator is given by an inverse exponential power law of the form given in equation (7.14) (see also 2.3).

$$I = I_0 e^{-\mu t} \quad (7.14)$$

In this equation I_0 is the intensity of the photon beam before the collimator, t is the transmission length and the coefficient μ is the attenuation coefficient. The value of this attenuation coefficient is not equal for all considered photon energies in the range from 2.3 - 6 MeV. The value which was used was taken from the NIST database [18] and is $4.3 \cdot 10^{-2} \text{ cm}^{-1}$. It is a mean value over the considered photon energy range.

For the points x_2 , which do not have a direct view of the detector, an exactly analogue calculation was done, except that the angles for which a photon would hit the detector were changed. These angles α_4 and α_5 are given in equations (7.15) and (7.16) (see figure 7.15).

$$\tan(\alpha_4) = \frac{r}{x_2 + \frac{d}{2}} \quad (7.15)$$

$$\tan(\alpha_5) = \frac{r}{x_2 - \frac{d}{2}} \quad (7.16)$$

For the points x_2 the probability for a photon being emitted in the direction of the detector and then the probability for this photon to reach the detector through the collimator needed to be calculated. This is done completely analogue to the points x_1 .

Now the sum over the 3 different probabilities mentioned above had to be formed: one for the points x_1 for a photon hitting the detector without penetrating the collimator, which was calculated in section 7.2. And the 2 probabilities for the points x_1 and x_2 for photons hitting the detector after penetrating through the collimator (which are attenuated according to the mentioned inverse exponential power law), which were calculated above. This sum yields a probability distribution shown in figure 7.16. In this and in following figures, the thickness of the collimator is 2 mm and the length is 3 cm and the radius of the detector is 50 cm.

This calculation needed to be verified. To do that a point like gamma ray source was put inside the detecting setup consisting of collimators and detectors, which is for example shown in figure 7.14. From this setup, the carbon source and the target were also

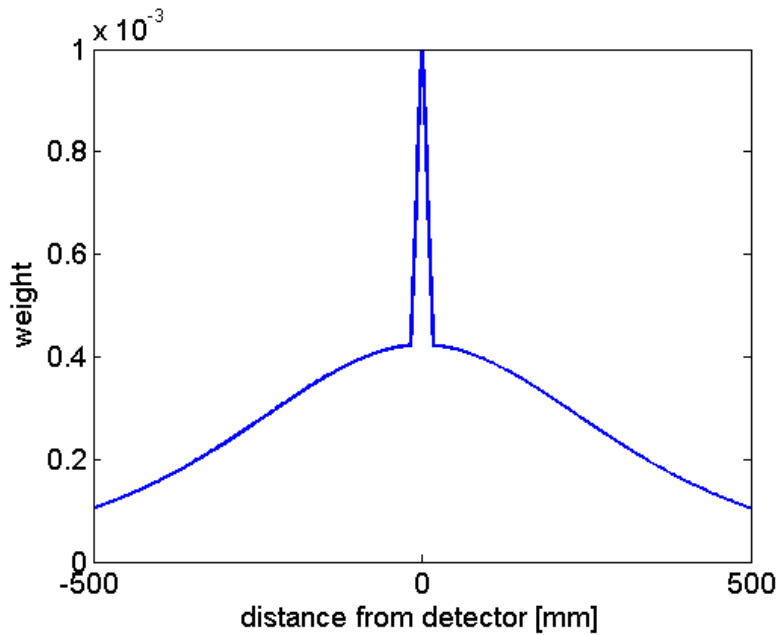


Figure 7.16: Probability distribution for a photon hitting a detector some distance away from its origin for isotropic photon production in the beam and a detector setup with lead collimators.

removed. The latter to avoid scattering effects inside it, because the response function without the scattering inside the target was of interest at this point. The gamma ray source emitted photons in the energy range from 2.3 - 6 MeV, the same energy range which the detectors also were sensible for. Additionally the photons were emitted isotropically. The energy distribution was a Gaussian curve, with a mean of 1 MeV and a sigma of 5 MeV, from which only the energy range from 2.3 - 6 MeV was taken. This resulted in an energy distribution which was decreasing with increasing energy. A fact, which is also true for the photon energy distribution inside the target, which was roughly modelled.

This setup was built to find out the probability to detect a photon emitted by a point source (which is the number of detected photons for one detector divided by the number of photons emitted by the source) as a function of the distance between the source and the detector. This is exactly what the response function also does. It represents the probability of one photon emitted a distance x away from the detector to hit this detector. This is the same probability as the probability that a photon from a point source hits a detector the same distance x away. This is why the distance in the plots is sometimes marked “distance form detector” or “distance from source”, because these two formulations are interchangeable. Consequently, this simulation should yield the same probability as the

calculated response function. In figure 7.17, a comparison between the calculated and the simulated convolution function is given. It can be seen that the agreement between the

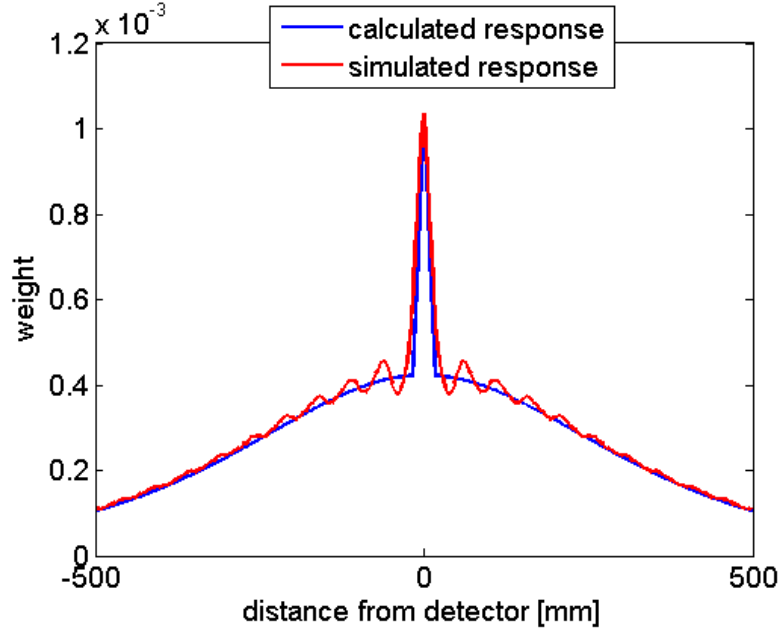


Figure 7.17: Comparison between the calculated and the simulated probability for a photon hitting the detector some distance away from its origin for a detector setup with lead collimators.

2 response functions is relatively high. Consequently, the estimation done to get to the calculated function were valid in general. But the fluctuations of the red curve compared to the blue curve are a consequence of this estimation, because the transmission length t was not calculated for every point correctly but rather as a mean path for the area where the point x was lying. This is where the difference comes from.

The asymmetry of the photon production also had to be taken into account. Until now, it was assumed, that the photon production was symmetric. This is not entirely true, as was mentioned before. More photons are produced in beam direction than opposite to the beam direction. This effect can for example be seen in figure 7.18. Here the produced photons with a momentum in beam direction and opposite to the beam direction (both multiplied by 2 to better compare it with the complete photon production) and the whole photon production for 240 MeV/u primary carbon ions in water can be seen. It is obvious that more particles in front of the Bragg peak are produced in beam direction than opposite to it. This had to be considered when calculating the response function. To calculate one point of the convolution, the amount of photons produced in one arbitrary point in

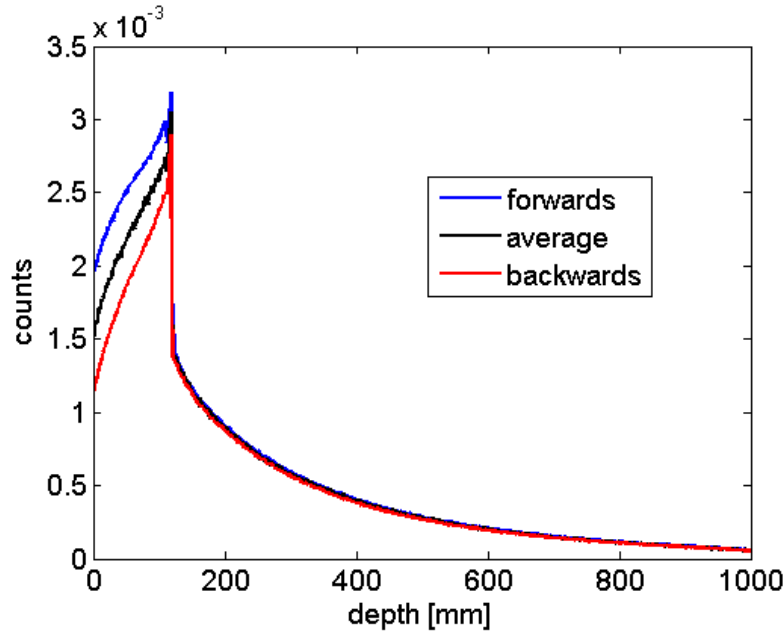


Figure 7.18: Photon production in different directions for carbon ions impinging on a water target at 240 MeV/u (data received from BSc. Dominik Steinschaden).

the target is taken and multiplied with the probability that one of these photons is detected by the detector at the point the convolution is currently calculated for. Then the sum over all points in the target is formed. As more photons are produced in beam direction, the probability for a photon hitting a detector further in beam direction is higher than for a photon hitting a detector opposite to the beam direction. As the response function is exactly this probability, it had to be changed due to this asymmetry. To visualize this effect, one can take a look at figure 7.22.

To adapt the response function, the ratio was calculated between the photons produced in forward direction (relative to the beam) to the photons which would be produced in forward direction with isotropic photon production (simply half the total counts). The same was done for the backward direction. This was done for each measured point (every millimeter) in front of the Bragg peak and the mean of all these values was taken. The outcome of this calculation for the photon production of carbon ions hitting a water target at 240 MeV/u was 1.15 (forward direction) and 0.85 (backward direction). Additionally the ratio between the photons, which can hit the detector directly (for the mentioned geometry with 3 cm collimator length, 2 mm collimator thickness and a detector radius of 50 cm, these are photons which are emitted approximately between 88° and 92° relative

to the beam) and the photons which would be produced in this direction with isotropic photon production was calculated. This ratio turned out to be 0.94. Then the respective points of the response function were multiplied with these values. This yields a convolution function, with a higher probability of an arbitrary photon to hit a detector in beam direction than opposite to the beam direction and a slightly lower chance for a photon to hit a detector right above its place of production compared to isotropic photon production. The changed response function is shown in figure 7.19. Of course this scheme to

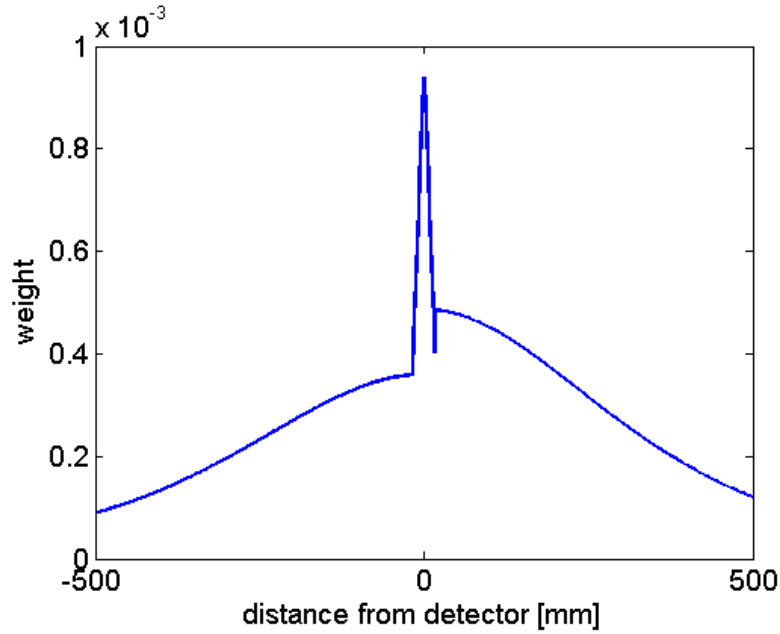


Figure 7.19: Response function for a detector setup with lead collimators taking into account asymmetry of photon production.

improve the response function is again a bit of an approximation, because it means that photons are produced 1.15 times as much for every angle in forward direction compared to isotropic production, which is not entirely true, but a good approximation. Furthermore, the values for the factors 1.15 and 0.85 were taken for 240 MeV/u primary carbon ions in water. They are not necessarily the same for all energies and for all materials. For example, for 400 MeV/u primary carbon ions in water, the mentioned values are 1.17 and 0.83. But as it is the case for every investigated material and primary ion energy, that more photons are produced in forward direction than in backward direction, the effect should be taken into account in the derivation of the response function.

Effects in the target also have to be considered in the response function. To look at these effects isotropic photon radiation is considered again. In the target scattering and

absorption of photons takes place. On the one hand, photons from the interesting energy range (2.3 - 6 MeV) get absorbed or lose enough energy through scattering processes to be below 2.3 MeV and consequently are not detected in this energy range. On the other hand, photons which are produced with a higher energy than 6 MeV, also lose energy through scattering and consequently have the possibility to be detected in the energy range from 2.3 - 6 MeV. To get a feeling for the strength of these effects, similar simulation as before were done. The simulation setup was the same as in figure 7.14. This time, the carbon ion source was removed but not the target. And an isotropically radiating gamma source was put right in the middle of the target. The target was a water cylinder with a length of 1 m and a radius of 30 cm. Again, photons in the area of 2.3 - 6 MeV were counted by the detectors, which were situated in between collimator rings.

At first, the source emitted photons in the interesting energy range. This was done to see how strong the scattering and absorption effects were in the target. Then the source emitted photons with higher energy, from 6 - 15 MeV. Also for the higher energy photon source, the mean of the energy distribution was 1 MeV and the standard deviation was 5 MeV, resulting in production rate decreasing with increasing energy in the energy range from 6 - 15 MeV, which was taken out of this distribution. All this was done to see how many detected photons in the range from 2.3 - 6 MeV originate from higher energy photons. The results of these simulations are shown in figure 7.20. The blue line in the plot represents the detected photons with the 2.3 - 6 MeV source. One can see that it lies far beneath the dark green line (roughly 40 %), which represents the photon counts recorded without scattering in the target (it is the same line as in figure 7.17). The red line on the bottom of the picture represents the photon counts in the lower energy range, per photon produced in the energy range from 6 - 15 MeV. Consequently for every photon produced in this energy range, about 10^{-4} photons of the lower energy range hit the detector right above the place of production. This scattering effect poses a bit of a problem for the convolution. A convolution, as it is used in this work, links the photons produced in one energy range to photons detected in the same energy range. But due to the mentioned scattering effect photons produced with high energy also have to be linked to photons detected with low energy. To solve this problem the rough estimation was made that for every photon in the interesting energy range, one photon in the higher energy range is produced. As the spectrum of the photon production depends on the depth of the target (see [17]), this is only true on average (and then only roughly) and not for every point inside the target. But since the detected photons per produced high energy photon are low compared to the detected photons per produced photon in the range from 2.3 - 6 MeV, this estimation does not yield a big error.

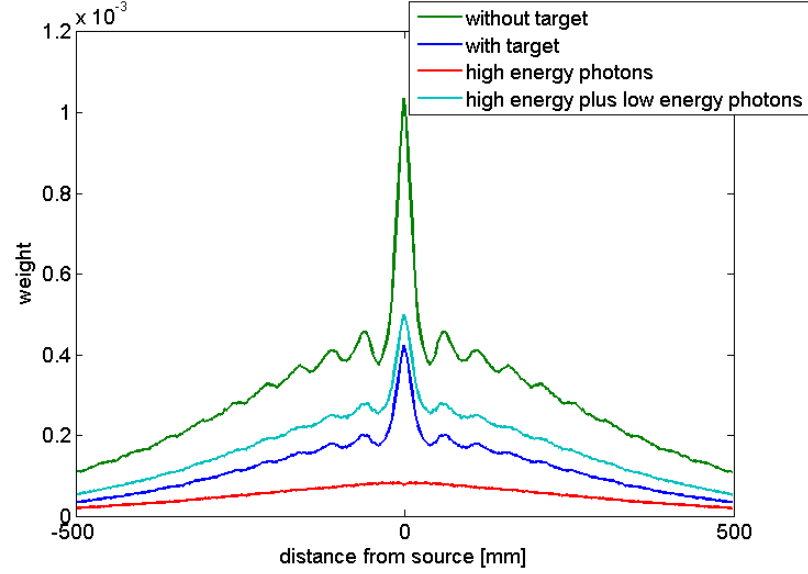


Figure 7.20: Photon detection probability in the energy range from 2.3 - 6 MeV for different simulation setups.

If one wants to know how many photons are detected in the interesting energy range per produced photon in the same energy range at a given distance from the center of production, the probability that a photon gets there through target and collimators (blue line in the plot) has to be taken. And the probability, that the one photon that is produced in the high energy region (according to the estimation it is exactly one photon), gets scattered down and hits the detector (red line in the plot) has to be added. These 2 probabilities add up to the light blue line in the plot.

So this light blue line should be a good estimation for the final response function for this setup and isotropic photon production. But the problem is, that this function is just simulated, which is not possible in real applications. In these circumstances, this function has to be calculated in advance. To do this, it is instructive to look at figure 7.21. The red curve represents the ratio between the simulated response function with the water target and the calculated response function without any attenuation effects. This factor gives information about the attenuation of the photons due to effects in the target. These effects could again be modelled with an inverse exponential power law and the attenuation coefficient for water. But this is a problem, because the attenuation coefficient for water varies greatly in the considered energy region.

Another problem is that the attenuation coefficient gives information about how many

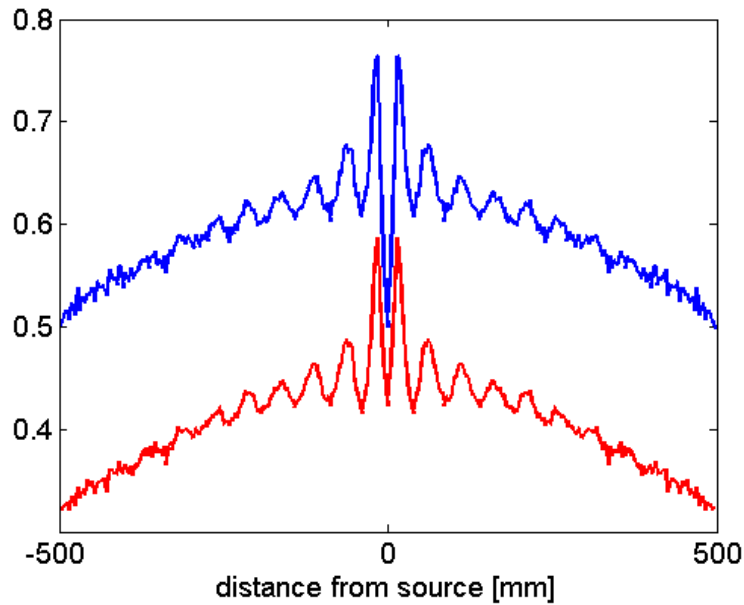


Figure 7.21: Ratio between the simulated response function with a water target and calculated response function without water target for a detector setup with lead collimators.

photons are still detected after an obstacle inside of a narrow particle beam, meaning they neither experience absorption nor scattering. Consequently not only absorbed photons are counted as lost, but also scattered photons. But in these simulations, the scattered photons can still be detected, because of the geometry of the detectors. In general, an attenuation coefficient for these simulations will consequently be lower than the values given in books. But nevertheless, the red curve is decreasing to the outside, which means it decreases with increasing distance to the source. This means that the attenuation in the target gets stronger with increasing distance which the photons have to travel through the target, which was to be expected. As a consequence the approach of modelling this effect with an inverse exponential power law with a yet unknown coefficient similar to the one in equation (7.14) was tried. This time, the t in this equation stands for the distance the photons travel through water.

The blue line in figure 7.21 represents the ratio between the simulated probability distribution for the detection of photons from 2.3 - 6 MeV coming from a source in this energy range plus those coming from a higher energy photon source (light blue line in figure 7.20) to the calculated response function. As this light blue line in figure 7.20 is an estimation for the real response function, the blue line in figure 7.21 is a good estimation for the

factor the calculated response function needs to be multiplied with to get to this real response function. As this factor again decreases with increasing distance to the source, and as a big part of it comes from attenuation in the target, it is modelled with an inverse exponential power law of the form given in equation (7.17).

$$I = I_0 e^{-\mu t} \quad (7.17)$$

Again, t stands for the distance the photon has to travel through the target in a straight line to come from its origin to the detector and is defined in equation (7.18).

$$t_{\text{Water}} = \frac{r_{\text{Target}}}{r_{\text{Detector}}} \times \sqrt{r_{\text{Detector}}^2 + x^2} \quad (7.18)$$

t depends on the radius of the target and the detector (r_{Target} and r_{Detector}) and on the distance between photon origin and detector x . 3 factors contribute to this factor μ :

First: The absorption and scattering in the target. The value for μ for this effect can be looked up in books (it is about 0.035 cm^{-1} for the considered energy range; value taken again from the NIST database [18]).

Second: The effect that some scattered photons are still detected. This effect leads to a reduction of this value.

Third: Photons, which are produced in a higher energy range lose energy and are detected in the energy range from 2.3 - 6 MeV. This also leads to a reduction of this value.

Finally to get to the final response function, this parameter μ had to be calculated. For this purpose the response function, which takes into account the anisotropy of the photon production is considered again. The purpose of the response function is to link the photon production with the photon detection. As this is the case, the ideal response function is the one for which the convolution of the response function with the photon production yields the detected photons. Consequently the μ factor had to be fitted according to this condition. This was done with the Matlab function `nlinfit`. This function conducted a least squares fit of the convolution of the photon production with the calculated response function, which was multiplied by a factor $e^{-\mu t}$ (t again standing for the distance the photon travels through water), to the detected photons. The fitted parameter here was μ . The exponent was fitted to the value of 0.0078 cm^{-1} , which is in good agreement to the considerations above.

A thing that has to be said about the response function is, that there is not one correct response function. This is the case, because the emission of photons as a function of

the angle α inside the target changes with depth. This effect is most prominent at the Bragg peak, where this behaviour changes from more photons being produced in forward direction than in backward direction in front of the Bragg peak to almost isotropic production after the Bragg peak. As the value of the response function at some point is the probability that a photon is produced in the direction of the detector times the probability that it then actually gets there, this effect also changes the response function. Therefore the values of this function would have to change when calculating the convolution for different depths. Consequently every attempt to conduct the fits mentioned in the next section with just one response function can always be just an approximation. Every time that it is mentioned in the following text, that the response function is not perfect, this effect is meant. This effect can be visualized with figure 7.22.

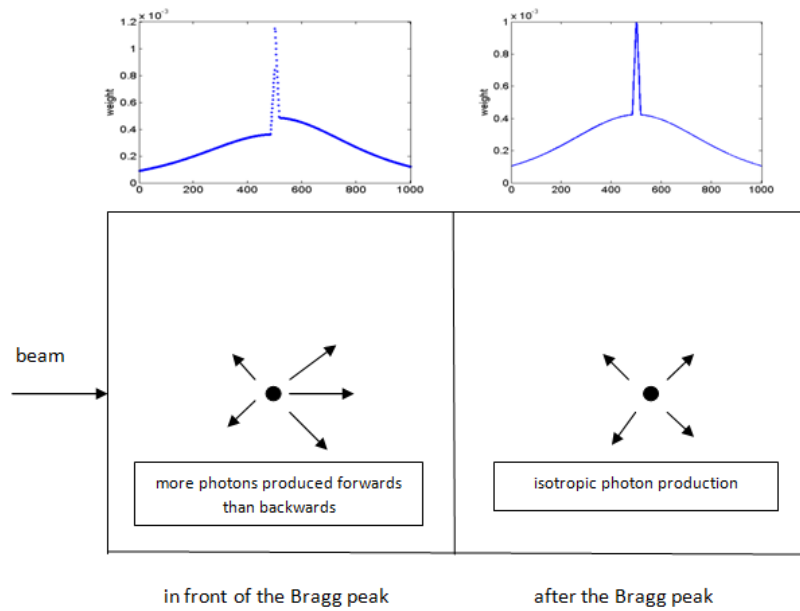


Figure 7.22: Variation of the response function with depth.

7.3.2 Calculation of the Bragg peak

This section is similar to section 7.2.2. The general strategy of fitting the convolution of a model function with a calculated response function to the detected photons stays the same. One thing that was changed was the model function for the photon production. In the previous chapter it used to be 2 straight lines with a jump in between them. To better suit the photon production in the energy range from 2.3 - 6 MeV, this was changed

to the function given in equation (7.19).

$$f(x) = (k_1 x^{\alpha_1} + d_1) \times H(x_{\text{Bragg}} - x) + (k_2 x^{\alpha_2} + d_2) \times H(x - x_{\text{Bragg}}) \quad (7.19)$$

In this equation, the function H is the Heaviside step function. It ensures that the first part of the function is zero behind the Bragg peak position (x_{Bragg}) and that the second part is zero in front of this position. Furthermore x is the position inside the target. Now there are 7 variable parameters in this model, namely: $k_{1,2}, d_{1,2}, \alpha_{1,2}$ and most important of all x_{Bragg} , the position of the Bragg peak. This kind of function was chosen because with the right set of parameters, the photon production in the studied energy range can be modelled very well.

The starting values s for this function were calculated like in equation (7.20).

$$s = t(1 + rand) \quad (7.20)$$

Here t represents the true value, which had been calculated in advance, and $rand$ is a random number picked from a normal distribution with mean 0 and adjustable standard deviation. This standard deviation was chosen to be 0.4 in most cases. These values were the starting values for a fit with the Matlab function `lsqnonlin`. This function convoluted the model function created with the input parameters with the response function and compared the result to the detected photons. Then it changed the 7 model parameters as long as either the sum of the squares of the difference between the 2 functions was below a threshold or the maximum number of iterations was reached (see also figure 7.11 in the previous section). Another feature of the `lsqnonlin` function is, that one can specify upper and lower limits for the fit parameters. The upper and the lower limits l were calculated like in equation 7.21.

$$l = t(1 \pm tol) \quad (7.21)$$

t is the true value and the tolerance tol was taken to be 0.6. This was done to prevent the fit from drifting off in wrong regions for the values. The resulting values of this fit were then given to the Matlab function `nlinfit` as starting values. This function again calculated a fit, this time without the limits for the values. And this function also determined 95 % confidence intervals for the fitted parameters. The 2 successive fits were made in order to get good starting values and also confidence intervals for the fitted parameters.

It was mentioned before that the behaviour of the production of the photons changes at the Bragg peak and with this, also the values of an ideal response function. As one can see from figure 7.22, the anisotropic response function, which was used for these fits, is only valid for points in front of the Bragg peak. To minimize errors coming from the

change of the response function with depth, only the detector points from the beginning of the target until slightly after the Bragg peak were used to calculate these fits.

7.3.3 Optimization of the geometry

After determining the new response function, optimal dimensions for the lead collimators had to be found. The general geometry of rings made of lead going around the target in circles with detectors in between them (geometry see figure 7.14) was not changed. Optimal configuration in the sense, that it is possible to determine the Bragg peak as exactly as possible with the signal of as few primary particles as possible. Also the target geometry was not changed, meaning a water cylinder with a radius of 30 cm and a length of 50 cm was used. The primary carbon ion energy was set to 240 MeV/u. Furthermore, the photons in the energy range 2.3 - 6 MeV were used. The number of primary ions was set to $4 \cdot 10^8$, in order to get high statistics. All this was done of course to be able to detect the Bragg peak in a real world application as fast as possible and with that spare the patient of unnecessary dose deposited in the wrong position. This optimization was not done to perfection and there is still much work to do in this field.

In the beginning collimators with a thickness of 9 mm and with their length varying from 2 cm to 5 cm were investigated. In between these collimators, at a radius from the beam line of 50 cm, at the end of the collimator rings, the detector was placed with a width of 1 mm. As a first indication of the optimal geometry, the counts of the detected photons in the mentioned energy range were investigated. The results are shown in figure 7.23. In this plot, the black line marks the Bragg peak. The count rates are decreasing with increasing collimator length. This was expected as longer collimators mean more absorption which results in decreasing count rates. This is why in order to get the highest count rate possible, short collimators would be the best solution. Additionally, the point of the highest number of detected photons is always slightly before the Bragg peak. This effect can be reproduced by the convolution of the photon production with the response function. This rise is an indicator of the Bragg peak position and thus very important. In the plot, it seems to be most significant for the 3 cm and 4 cm collimators. For the 2 cm collimators, this rise in the counts is very small, which is due to lack of absorption in the collimators and a resulting loss of information about the place of production of the detected photons. These facts indicate that a 3 cm or 4 cm long collimator might be a good choice.

To support this choice, the Bragg peak starting from the detected photons for each configuration needed to be calculated. To do that, the response function for every configuration

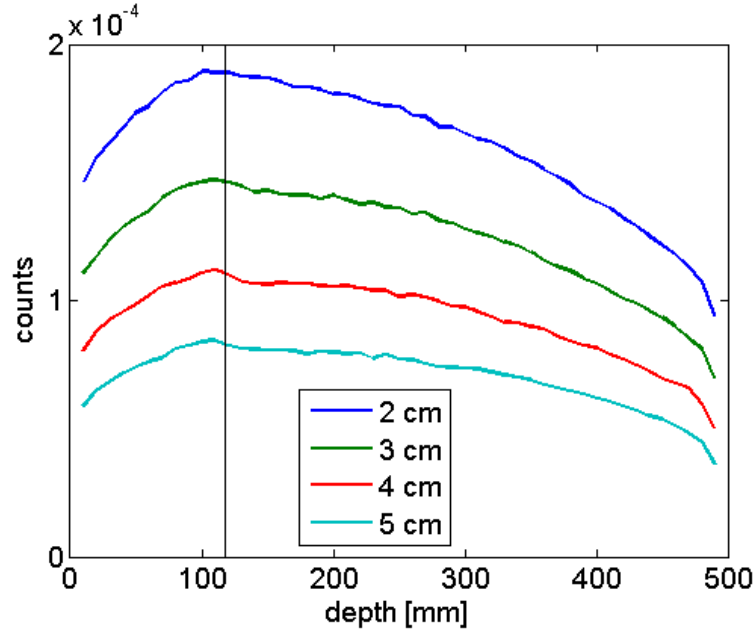


Figure 7.23: Detected photons in the energy range from 2.3 - 6 MeV for different collimator lengths for carbon ions impinging on a water target at 240 MeV/u.

was computed as shown in section 7.3.1. This function was put into the fitting routine described in section 7.3.2, which then calculated the fit of the photon production and with that the Bragg peak position with confidence intervals. Of course, the exact outcome of one of these fits depends on the starting values of the fitting routine, which are changed for each single fit, but the changes are not significant. A typical result is shown in figure 7.24. In this picture, the blue points are the fitted values for the Bragg peak depth and the error bars represent the calculated value plus/minus one standard error. The standard error is calculated from the 95 % confidence interval given by the fit by dividing the whole interval through 2 times the critical-t-value for the student-t-distribution of $n - 7$ degrees of freedom, where n is the number of detector points the fit compares the convoluted function to ($n = 49$ in this case). And $n - 7$, because there are 7 fitted parameters. For this situation, the critical-t value is about 2.02. As the true value for the Bragg peak is 118 mm for this primary energy in water, one can see that also 3 cm and 4 cm collimator length are closest to it. Of course this scheme should work for every detector and collimator configuration, but the fact that the fit yields wrong values for some of them, is due to instability of the fit because of either not enough detected particles or the rise in the count rates not being significant enough. Because of the higher count rates and along with that, better statistics compared to the 4 cm collimator, the 3 cm collimator was chosen.

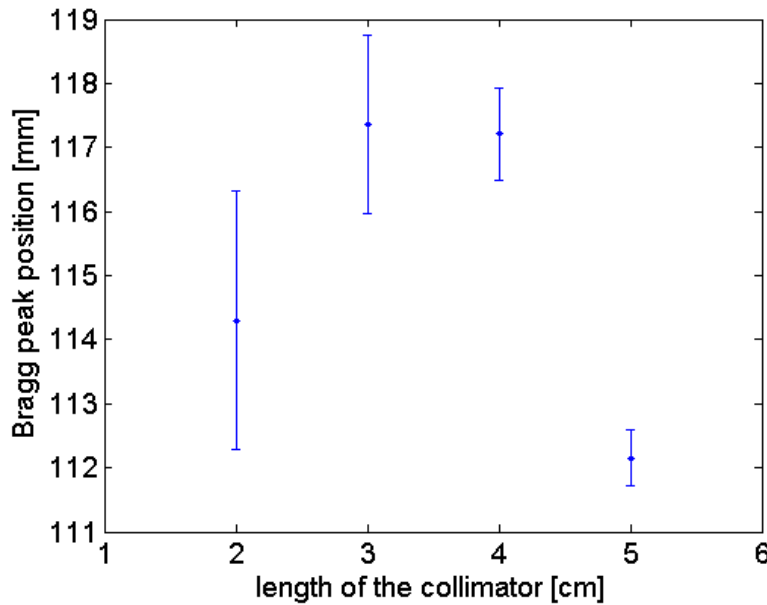


Figure 7.24: Calculated Bragg peak position for different collimator lengths for carbon ions impinging on a water target at 240 MeV/u.

The next thing which needed to be varied was the collimator thickness. For the length of 3 cm, which was chosen for the reasons given above, 2 mm and 4 mm thick collimators, apart from the 9 mm thick collimators which were already mentioned, were tried. The detector width was still set to 1 mm. The counts for these detector and collimator configurations are shown in figure 7.25. Again, these plots are from data acquired with $4 \cdot 10^8$ primary ions.

As expected, the smallest collimator thickness yields the highest count rates and vice versa. This data is shown only until 280 mm, because the data of the area of the Bragg peak is the most interesting, because it contains the rise of the count rate which can be linked to the peak. Also it was mentioned above that the fitting routines only took into account the detectors from the beginning until shortly after the Bragg peak, for reasons given above.

To decide which collimator configuration is the optimal one, the response functions for all of these configurations had to be calculated and afterwards the fits had to be carried out to determine the Bragg peak position and error bounds. The results are shown in figure 7.26. It is obvious that all the collimator geometries yield an estimation for the Bragg

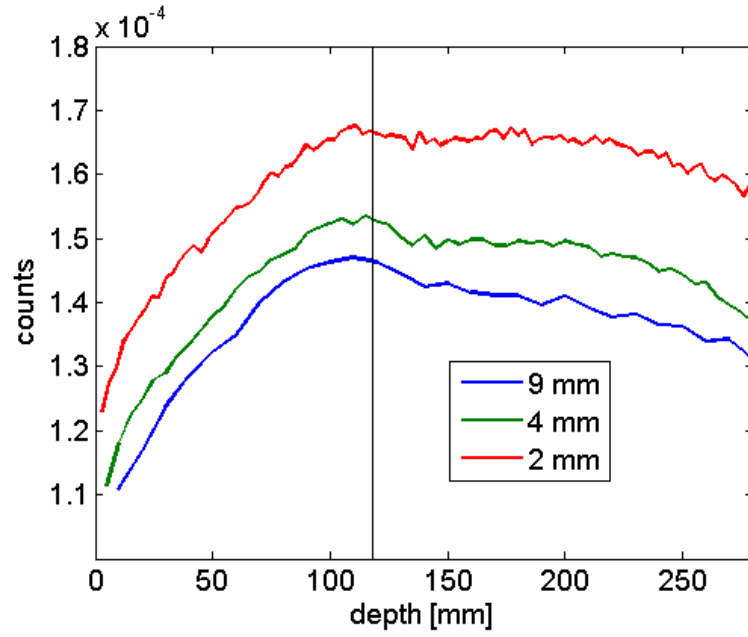


Figure 7.25: Detected photons in the energy range from 2.3 - 6 MeV for different collimator thicknesses and for carbon ions impinging on a water target at 240 MeV/u.

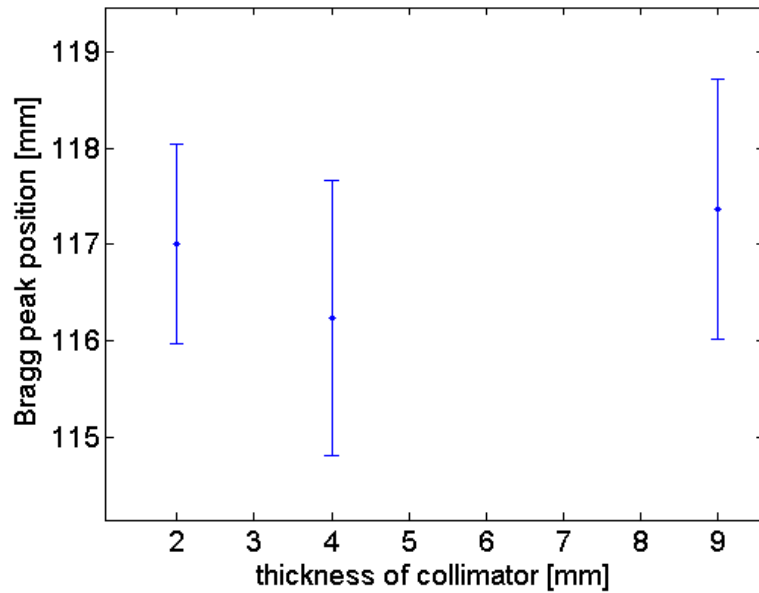


Figure 7.26: Calculated Bragg peak position with error bounds for different collimator thicknesses and for carbon ions impinging on a water at 240 MeV/u.

peak position, which is close to the real value of 118 mm. Also the error bounds are of the same size. Again it has to be said that these are the results for one fit. These results can vary slightly depending on the initial values for the fitting routine, which are chosen independently for every fit. Or on the exact number of detectors, the fitting routine takes into account for the calculation. As the collimator thickness is different for these 3 setups, the distance between 2 detectors is also different, because this distance is exactly the collimator thickness. Consequently the lowest collimator thickness has the highest number of detectors on the same length. The fits above were all calculated by taking into account the same length, which means for the smallest thickness, the most detectors contributed to the result. For these reasons (Bragg peak value close to reality, most detectors contributing to the fit for same length and highest count rate), the collimator geometry with 3 cm long and 2 mm thick collimators was chosen.

7.3.4 Results for different primary ion energies

Now this scheme was applied to different primary ion energies and different primary ion numbers. This information was needed in order to get a knowledge about how many primary particles would be necessary to determine the Bragg peak position. This information is crucial, because it is important in a real world application to get the information about the dose distribution as fast as possible in order to spare the patient of unnecessary dose. The target was the same as before, a water cylinder with a radius of 30 cm and a length of 50 cm. The response function was the same for all energies. It is the one shown in figure 7.19, multiplied by a factor which should model attenuation effects in the target. This function is shown in figure 7.27.

To get the results for different primary ion numbers, 5 different simulations with the same simulation setup and with a primary ion number of $8 \cdot 10^7$ particles were conducted. Then to get for example data for $2.4 \cdot 10^8$ primary particles, the data of 3 of these simulations were combined, picking the number of the simulations (1-5) randomly, but never picking 2 times the same simulation for one fit.

The first investigated primary energy was 240 MeV/u, the one which was investigated until now. In figure 7.28 one can see a typical fit to the photon production, where the fit has been done analogue to the procedure described in section 7.3.2. This and the following figures of this kind were all acquired with $4 \cdot 10^8$ primary ions. The green line indicates the initial guess for the photon production, the blue line the final fit to the photon production and the red line indicates the real photon production. One can see that the part after the Bragg peak is fitted quite well, while the part in front of the Bragg peak is not so

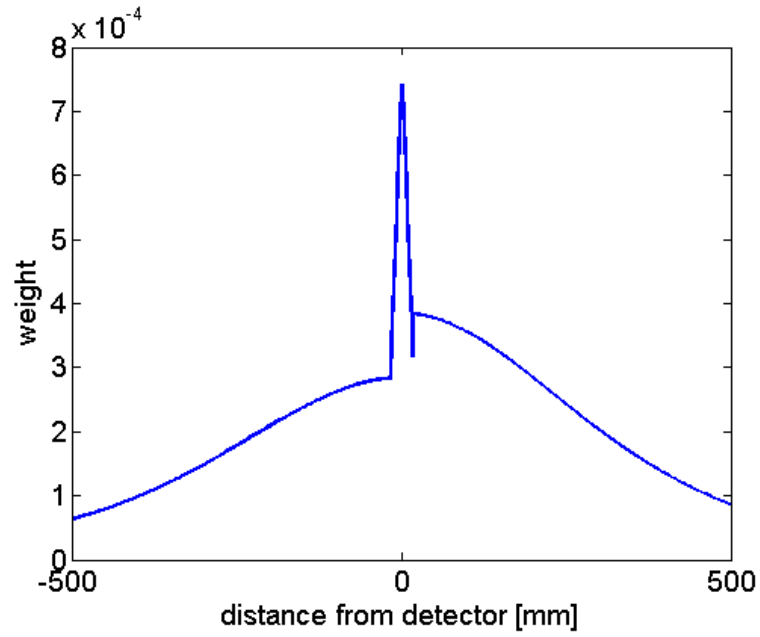


Figure 7.27: Response function for a certain target and detector geometry (explanation see text).

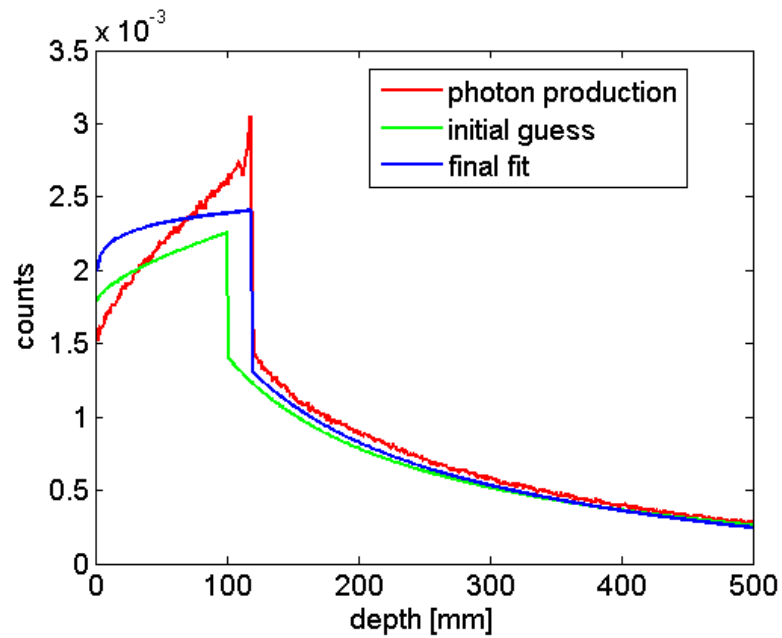


Figure 7.28: Photon production with fit for carbon ions impinging on a water target at 240 MeV/u.

accurate. The reason for this is again an imperfect response function. In figure 7.29, one

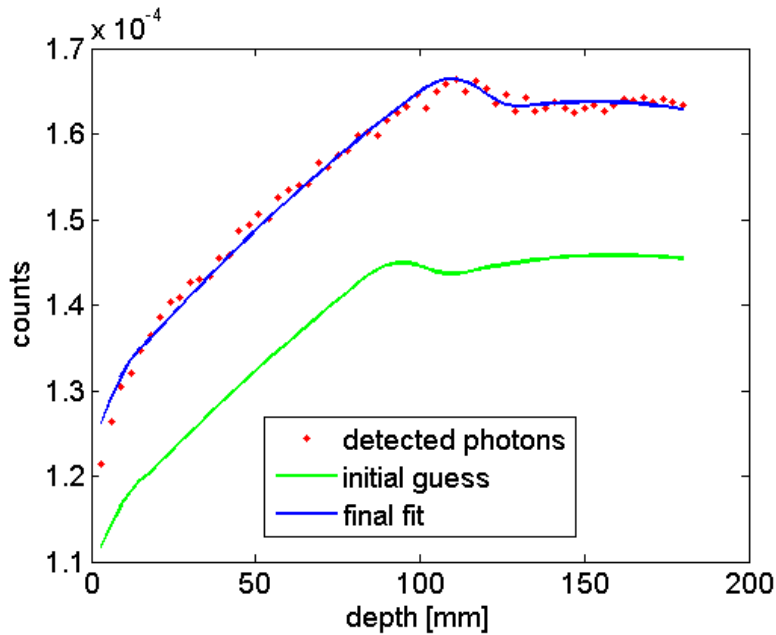


Figure 7.29: Photon detection with fit for carbon ions impinging on a water target at 240 MeV/u.

can see the photon detection (red dots) and the convolution of the initial guess (green line) and the final fit (blue line) of the photon production with the response function. The agreement between the measurement and the fit is really high, as can be seen in the picture. Here only the data which were used by the fitting routine is shown.

In figure 7.30, the outcome of the fit for different primary ion numbers is shown. Again it has to be said that the exact outcome of a fit depends on the initial conditions, which vary slightly and also now on which of the 5 simulations (simulation numbers 1-5) are used to get to the result. But these effects are not significant. For the highest primary ion numbers, the fit returns the true value for the Bragg peak position and the highest deviation of 2 mm occurs for the smallest primary ion number. Furthermore one can see that the outcome of the fit does not depend heavily on the primary ion number, therefore it should be possible to determine the Bragg peak even with the smallest investigated primary ion number of $8 \cdot 10^7$ particles. But nevertheless, the standard error is increasing for decreasing primary ion number, and consequently the accuracy of this scheme depends on the number of primary ions.

The same investigations were made for 120 MeV/u and 400 MeV/u primary ions. In

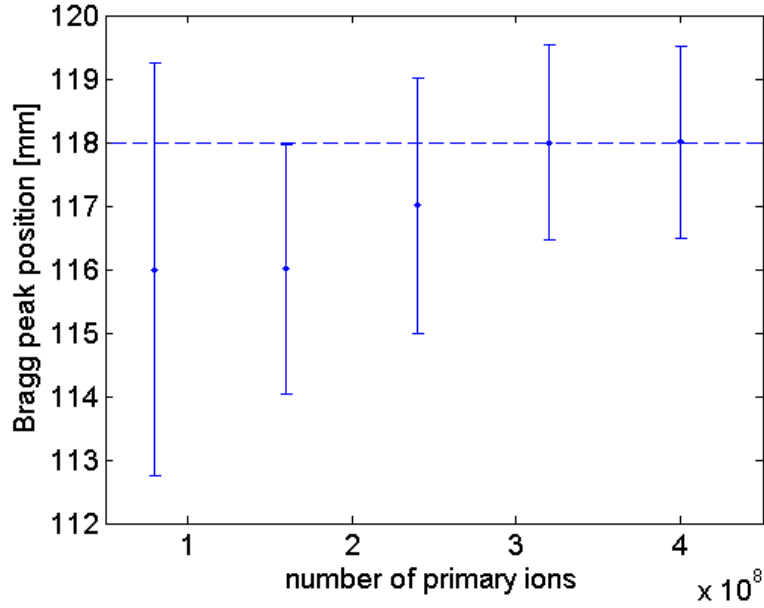


Figure 7.30: Fitted Bragg peak position with error bounds for carbon ions impinging on a water target at 240 MeV/u, the dashed blue line marking the Bragg peak.

figures 7.31 and 7.32, the results of the fits are shown. For the lowest energy, the Bragg peak position is overestimated slightly. For the highest primary ion energy, the Bragg peak position is underestimated by the fit. For these energies (120 MeV/u and 400 MeV/u), the investigations for different primary ion numbers were also made. The results are shown in figures 7.33 and 7.34. The true values for the Bragg peak depths are 35 mm and 274 mm respectively. For the lower energy, the peak position is overestimated by about 2 mm or about 5 %. For the higher energy it is underestimated. This time the mean value of the fits lies about 7 mm or 3 % under the true value. The standard error increases for both of these energies with decreasing primary ion number, which was expected because of the lower statistics. The standard error does in these plots not include the true value, as the imperfections of the response function yield a systematic error. The calculated Bragg peak depth with standard errors for 4×10^8 particles are summed up in table 7.2. Furthermore, the results for different primary ion numbers for all simulated primary ion energies are summed up in tables 7.3 - 7.5.

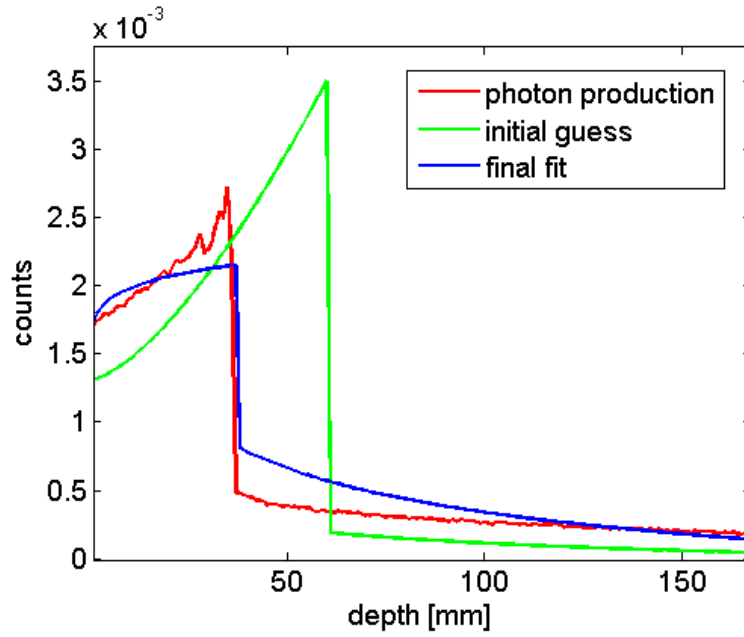


Figure 7.31: Photon production with fit for carbon ions impinging on a water target at 120 MeV/u.

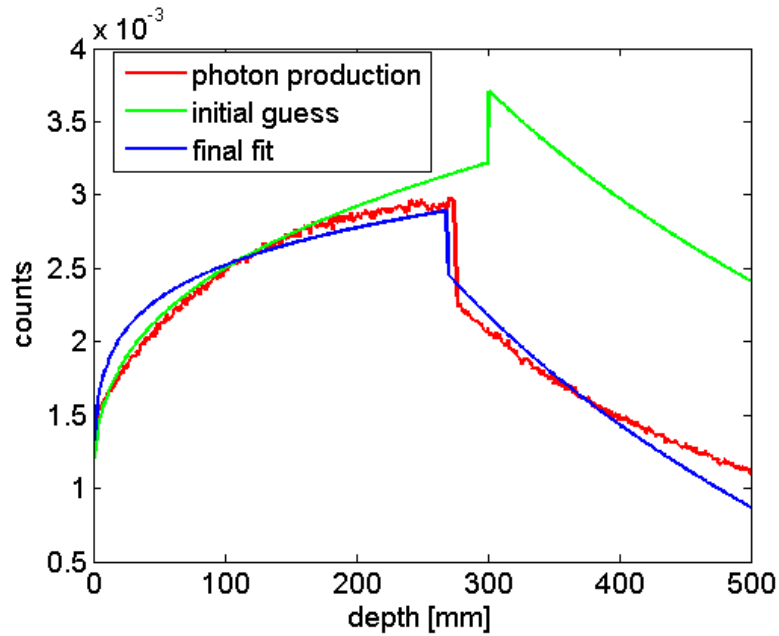


Figure 7.32: Photon production with fit for carbon ions impinging on a water target at 400 MeV/u.

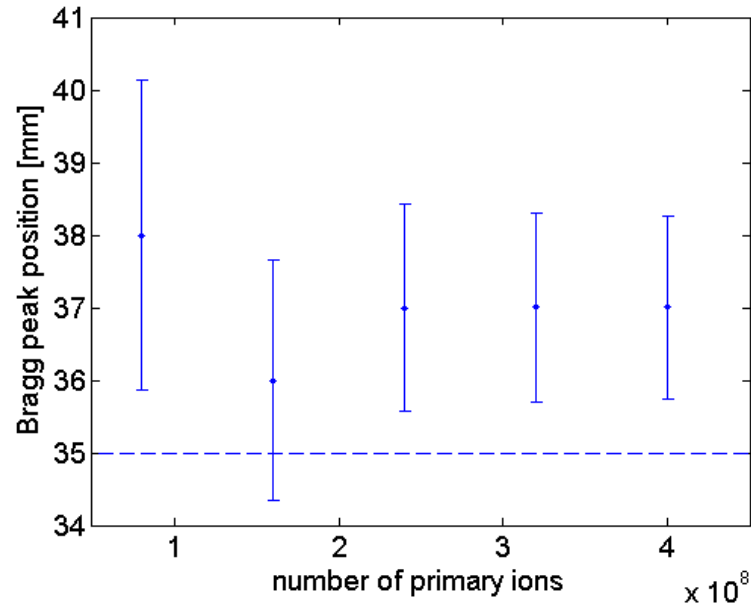


Figure 7.33: Fitted Bragg peak position with error bounds for carbon ions impinging on a water target at 120 MeV/u, the dashed blue line marking the Bragg peak.

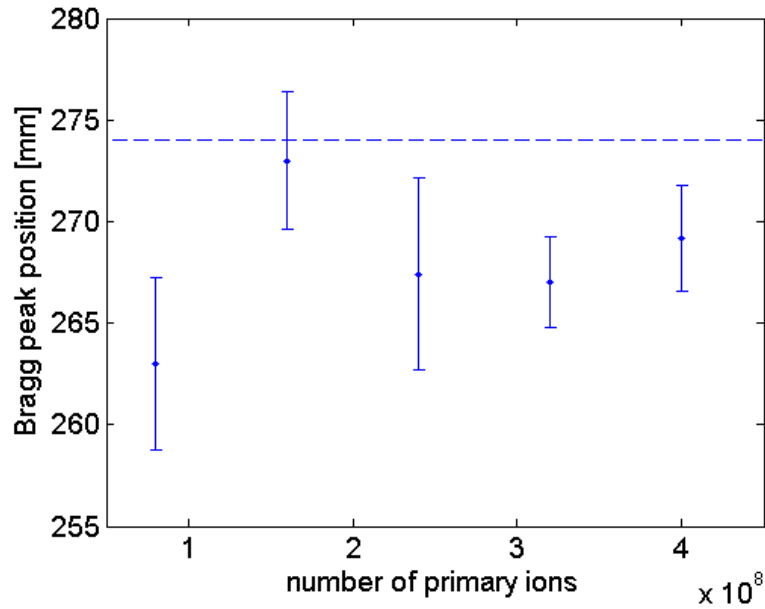


Figure 7.34: Fitted Bragg peak position with error bounds for carbon ions impinging on a water target at 400 MeV/u, the dashed blue line marking the Bragg peak.

energy [MeV/u]	fitted Bragg depth [mm]	true Bragg depth [mm]
120	37 ± 1.3	35
240	118 ± 1.5	118
400	269.2 ± 2.6	274

Table 7.2: Calculated and true Bragg peak depths for carbon ions impinging on a water target at several primary ion energies.

primary ion number	fitted Bragg depth [mm]	standard error [mm]
$8 \cdot 10^7$	38	2.15
$1.6 \cdot 10^8$	36	1.65
$2.4 \cdot 10^8$	37	1.42
$3.2 \cdot 10^8$	37	1.3
$4 \cdot 10^8$	37	1.26

Table 7.3: Calculated Bragg peak depths and error bounds for carbon ions impinging on a water target at 120 MeV/u for several primary ion numbers (true Bragg peak depth is 35 mm).

primary ion number	fitted Bragg depth [mm]	standard error [mm]
$8 \cdot 10^7$	116	3.25
$1.6 \cdot 10^8$	116	1.96
$2.4 \cdot 10^8$	117	2.02
$3.2 \cdot 10^8$	117	1.53
$4 \cdot 10^8$	118	1.52

Table 7.4: Calculated Bragg peak depths and error bounds for carbon ions impinging on a water target at 240 MeV/u for several primary ion numbers (true Bragg peak depth is 118 mm).

primary ion number	fitted Bragg depth [mm]	standard error [mm]
$8 \cdot 10^7$	263	4.26
$1.6 \cdot 10^8$	273	3.4
$2.4 \cdot 10^8$	267.4	4.72
$3.2 \cdot 10^8$	267	2.24
$4 \cdot 10^8$	269.2	2.64

Table 7.5: Calculated Bragg peak depths and error bounds for carbon ions impinging on a water target at 400 MeV/u for several primary ion numbers (true Bragg peak depth is 274 mm).

8 Summary and outlook

In the course of this work, the depth-dose distribution and with that the depth of the Bragg peak during carbon ion therapy has been measured for different materials and compared to experimental results with a maximum relative deviation of 4 %. Also the angle distribution of the prompt γ - photons has been measured with the outcome, that about 30 % more photons in the interesting energy range from 2.3 - 6 MeV are detected in beam direction than opposite to the beam direction. This fact was linked to a higher number of produced photons in beam direction. Furthermore a detector arrangement, consisting of cylindrical lead collimators and detectors, has been proposed for calculating the depth of the Bragg peak in beam direction with the help of a response function, which models the effect of the imperfection of the collimator. The Bragg peak depth could be calculated with a relative error of 0 % to 5 %, depending on the primary ion energy, for a cylindrical water target and a primary ion number of $4 \cdot 10^8$. The error was mainly caused by inaccuracies of the response function. As $4 \cdot 10^8$ is also the maximum number of primary carbon ions per pulse at MedAustron [9], it would be possible to detect the Bragg peak for the mentioned setup with the particles of one pulse with the accuracy given above. Consequently, the possibility to calculate the Bragg peak by detecting prompt photons was proven.

To build a detector like it was mentioned in the course of this work, several more steps have to be taken. These steps include the optimization of the detector geometry and of the response function. Furthermore a way for calculating the position of the Bragg peak in 3 dimensions has to be found. Also the scheme for calculating the Bragg peak position has to be tested for other target materials and shapes.

Bibliography

- [1] E. Testa et al. (2008): *Monitoring the Bragg peak location of 73 MeV/u carbon ions by means of prompt gamma ray measurements*, Applied Physics Letters, Volume 93, Issue 9
- [2] D. Schardt et al. (2010): *Heavy-Ion tumor therapy: Physical and radiobiological benefits*, Reviews of modern physics, Volume 82, Number 1, Pages 383 - 425
- [3] K. Parodi (2012): *PET Monitoring of hadrontherapy*, Nuclear Medicine Review 2012, Volume 15, Suppl. C, C 37 - C 42
- [4] G. Goretzki (2004): *Medizinische Strahlenkunde: Physikalisch-technische Grundlagen*, 2nd edition, Urban & Fischer publishing company
- [5] W. Demtröder (2005): *Experimentalphysik 3*, 3rd edition, Springer publishing company
- [6] U. Linz (2012): *Ion Beam Therapy*, Springer publishing company
- [7] K. Poljanc et al. (2005): *Teilchenbeschleuniger*, Institute of atomic and subatomic physics
- [8] W. Demtröder (2005): *Experimentalphysik 4*, 2nd edition, Springer publishing company
- [9] www.medaustrotron.at, (30.9.2013)
- [10] S. Jan et al. (2011): *GATE V6: a major enhancement of the GATE simulation platform enabling modelling of CT and radiotherapy*, Physics in Medicine and Biology, Volume 56, Pages 881 - 901
- [11] S. Agostinelli et al. (2003): *GEANT4 - a simulation toolkit*, Nuclear Instruments and Methods in Physics Research, Section A, Volume 506, Issue 3, Pages 250 - 303
- [12] www.opengatecollaboration.org, (27.9.2013)
- [13] http://wiki.opengatecollaboration.org/index.php/Users_Guide_V6.2, (1.10.2013)

- [14] Brun R. et al. (1996): *ROOT - An Object Oriented Data Analysis Framework*, AIHENP conference in Lausanne
- [15] L. Strasser et al. (2011): *Bragg peak shape parameters as a tool for improving the $\langle I \rangle$ -value estimation*, Romanian reports in physics, Volume 63, Number 3, Pages 651-675
- [16] <http://www.srim.org/>, (11.10.2013)
- [17] D. Steinschaden (2013): *Investigation of the prompt gamma ray emission for on-line monitoring in ion therapy*, Vienna University of Technology
- [18] <http://www.nist.gov/pml/data/asd.cfm>, (17.9.2013)